J. Fluid Mech. (2000), *vol.* 414, *pp.* 1–33. Printed in the United Kingdom

Direct numerical simulation of a supersonic turbulent boundary layer at Mach 2.5

By STEPHEN E. GUARINI[1], ROBERT D. MOSER[2] KARIM SHARIFF[1] AND ALAN WRAY[1]

[1]NASA-Ames Research Center, Moffett Field, CA 94035, USA
[2]Department of Theoretical and Applied Mechanics, University of Illinois, Urbana, IL 61801, USA

(Received 20 March 1999 and in revised form 21 January 2000)

A direct numerical simulation of a supersonic turbulent boundary layer has been performed. We take advantage of a technique developed by Spalart for incompressible flow. In this technique, it is assumed that the boundary layer grows so slowly in the streamwise direction that the turbulence can be treated as approximately homogeneous in this direction. The slow growth is accounted for by a coordinate transformation and a multiple-scale analysis. The result is a modified system of equations, in which the flow is homogeneous in both the streamwise and spanwise directions, and which represents the state of the boundary layer at a given streamwise location. The equations are solved using a mixed Fourier and B-spline Galerkin method.

Results are presented for a case having an adiabatic wall, a Mach number of $M = 2.5$, and a Reynolds number, based on momentum integral thickness and wall viscosity, of $Re_{\theta'} = 849$. The Reynolds number based on momentum integral thickness and free-stream viscosity is $Re_\theta = 1577$. The results indicate that the Van Driest transformed velocity satisfies the incompressible scalings and a small logarithmic region is obtained. Both turbulence intensities and the Reynolds shear stress compare well with the incompressible simulations of Spalart when scaled by mean density. Pressure fluctuations are higher than in incompressible flow. Morkovin's prediction that streamwise velocity and temperature fluctuations should be anti-correlated, which happens to be supported by compressible experiments, does not hold in the simulation. Instead, a relationship is found between the rates of turbulent heat and momentum transfer. The turbulent kinetic energy budget is computed and compared with the budgets from Spalart's incompressible simulations.

1. Introduction

The study of supersonic turbulent boundary layers has primarily consisted of experimental investigations with a few recent attempts at numerical simulation. The experimental measurements are limited to basic turbulence quantities and by the spatial resolution near the wall, among other difficulties. The simulations have been hampered by large cost and low Reynolds number. The goal of the present work was to identify similarities and differences between compressible and incompressible boundary layers, as well as to test the applicability of Morkovin's hypothesis and the strong Reynolds analogy.

1.1. *Background and motivations*

Though most flows encountered in nature and in aerospace applications are turbulent or partially so, turbulence remains one of the most elusive subjects in aeronautics. There is no general turbulence theory or model. With the addition of compressibility the turbulence problem becomes even more complex. For instance, in boundary layers at high Mach numbers, large temperature gradients develop between the wall region and the outer layer. These gradients result in large variations of mean fluid properties, such as viscosity, which result in significant changes in the Reynolds number across the wall-normal direction. As the Mach number becomes hypersonic, shocks may form, dilatation becomes important, and baroclinic terms may be significant.

To account for the effects of compressibility, many theories have been developed based on a weakly compressible hypothesis (see the review by Spina, Smits & Robinson 1994). The hypothesis is that, at moderate free-stream Mach numbers ($M \lesssim 5$ according to Morkovin 1962), dilatation is small and any differences from incompressible turbulence can be accounted for by fluid property variations across the layer. This has long been appreciated and is the basis of the Van Driest (1951, 1956) transformation and the Morkovin (1962) hypothesis. Morkovin postulates that in the weak compressibility regime normal stresses will obey the incompressible scaling when they are multiplied by the local mean density divided by the free-stream value. Even at moderate free-stream Mach numbers the fluctuating and turbulence Mach numbers are small and one would not expect eddy shocklets to be a predominant feature of the flow field. However, at higher free-stream Mach numbers the turbulent velocity fluctuations are more likely to be supersonic leading to increased compressibility effects. Further support for the weak compressibility assumption is provided by the fact that large-scale structures are convected at $0.9U_\infty$ (Spina, Donovan & Smits 1991) which results in a small relative Mach number between the large eddies and the mean flow. Finally, another measure of compressibility, the gradient Mach number (Sarkar 1995), is also small in the boundary layer. The gradient Mach number is based on the velocity difference across the scale of an eddy.

The validity of the weak compressibility theories in compressible boundary layers has been checked in a variety of experiments over the years (see these and the references therein: Gaviglio 1987; Smith & Smits 1993; and Eléna & Gaviglio 1993). However, in most experiments the data reported have been limited to simple turbulence quantities such as the mean and RMS velocity and temperature. Detailed correlation statistics needed to directly check the validity of Morkovin's hypothesis are only available from a few experiments. The data from the direct numerical simulations reported here provide an opportunity to evaluate these theories in more detail than has been previously possible.

1.2. *Previous simulations*

Although there have been numerous experimental investigations of the compressible turbulent boundary layer, there have been relatively few attempts at direct numerical simulation of this flow. To date there have been three such attempts known to us: (i) Guo & Adams (1994) and Adams *et al.* (1998); (ii) Rai, Gatski & Erlebacher (1995); and (iii) Hatay & Biringen (1995).

The simulations of Guo & Adams and Adams *et al.* had an isothermal wall at the laminar adiabatic wall temperature and, like the current simulations, used a method that transformed the spatially evolving boundary layer into a parallel, streamwise homogeneous flow. To obtain their transformed parallel shear flow, Guo & Adams

(1994) require that the spatial mean of the periodic simulation obey the parabolized time-mean equations. These equations contain streamwise derivatives of Reynolds stresses which are obtained by performing simulations at different downstream stations. This approach leads to forcing terms in the mean equations that are similar to those produced by Spalart's approach, except that terms involving the coordinate transformation are not present.

Guo & Adams (1994) and Adams *et al.* (1998) simulate boundary layers at three Mach numbers $M = 3$, 4.5 and 6. In Guo & Adams, these simulations were performed in relatively small spatial domains; in particular, for $M = 3$ the domain was 16 times smaller in streamwise by spanwise area than those reported here. The effects of these small domains is evident in their statistical results, most notably the two-point correlations. Such small domains introduce considerable uncertainty regarding the impact of the domain size on the dynamics of the boundary layer, though experience with the minimal channel (Jimenez & Moin 1991) suggests that basic statistical quantities such as turbulence intensities should be reasonably accurate. One of the major design considerations of the current simulations was to avoid the uncertainties associated with such small simulation domains.

Unlike the current simulations and those of Guo & Adams, Rai *et al.* (1995) simulated a true spatially evolving boundary layer. They simulated a very long streamwise domain from a laminar inlet, through transition to a fully turbulent boundary layer. This clearly avoids any uncertainties that might be associated with the approximate spatial growth treatment used here and in Guo & Adams, but the cost is that the spatial domain that must be simulated is spectacularly large. As a result, even with the extremely large problem size they were able to run (17 million nodes), Rai *et al.*'s resolution was over a factor of 3 coarser in the streamwise direction (measured in wall units) than the current simulations. Such coarse resolution introduces uncertainties that are different from those associated with the approximate spatial growth treatment. Simulations like that reported here, which can be run with much better spatial resolution, are useful for assessing the impact of the coarse resolution that must be used in a simulation like that of Rai *et al.*

Finally, Hatay & Biringen (1995) performed a parallel-flow boundary layer calculation at $M = 2.5$. However, the data they present suggest that the turbulence is not being sustained. Indeed, the turbulence intensities appear to drop significantly over the course of the simulation. It is possible that the Reynolds number of their simulation is too low to sustain turbulence. The authors quote a Reynolds number based on displacement thickness of $Re_{\delta^*} \approx 1000$, which corresponds to a momentum-thickness Reynolds number of $Re_{\theta'} \approx 140$. Fernholz & Finley (1980) call flows in the Reynolds number range of $300 \leqslant Re_{\theta'} \leqslant 6000$ transitional, based on an analysis of mean velocity profiles. While their definition of transitional flows does not preclude having sustained turbulence below $Re_{\theta'} \approx 300$, the Reynolds number in Hatay & Biringen's simulation is well below the lower limit of this range.

Clearly, the direct numerical simulation of a compressible turbulent boundary layer is a difficult undertaking, in which various compromises must be made to make the simulation practical. In the research reported here, we have pursued the most reliable compressible boundary layer simulation that we were able to do with current computation capabilities, choosing good spatial resolution and adequate domain size over true spatial evolution. Such a simulation allows a much more detailed analysis of compressibility effects in the boundary layer than has been previously possible. The current simulation will be described and analysed in what follows, which includes simulation details (§ 2), turbulence statistics (§ 3), Reynolds analogies

(§ 4), the turbulent kinetic energy budget (§ 5) and conclusions (§ 6). The details of the approximate spatial growth treatment are given in the Appendix.

2. Simulation details

The details of the current simulation are provided in this section. The parameters used in the compressible turbulent boundary layer simulation are compared with the incompressible boundary layer simulations of Spalart (1988); the incompressible channel simulation of Kim, Moin & Moser (1987); and the compressible boundary layer simulations of Guo & Adams (1994) and Rai *et al.* (1995).

2.1. *Simulation method*

One difficulty in performing compressible turbulent boundary layer simulations is that the streamwise direction is inhomogeneous. This precludes the use of periodic boundary conditions, and as a result FFTs, in this direction. Furthermore it necessitates use of a long entrance length for the flow to adjust from artificial in-flow conditions.

Several techniques have been developed to address one or both of these issues for incompressible flow (Spalart & Leonard 1987; Spalart 1988; Spalart & Watmuff 1993; Bertolotti, Herbert & Spalart (1992); and Lund, Wu & Squires 1998). Of these we utilize the one developed in Spalart & Leonard (1987) and Spalart (1988). Spalart recognized that the slow growth of the boundary layer in the streamwise direction makes it possible to treat the turbulence as approximately homogeneous in this direction. The slow growth is taken into account by using a coordinate transformation and a transformation of dependent variables as in multi-scale asymptotics. The result is a modified system of equations (Navier–Stokes plus some extra terms, which we shall call 'slow growth terms') that is homogeneous in both the streamwise and spanwise directions, and which represents the state of the boundary layer at a given streamwise location (or, equivalently, a given thickness). Using Spalart's method, the boundary layer can be simulated separately at each streamwise station. A detailed description of this method and the modified set of equations can be found in the Appendix.

The resulting equations are solved using a mixed Fourier-spectral and B-spline-Galerkin method (Guarini 1998). The dependent variables (specific volume, $\sigma = 1/\rho$; momentum, $\boldsymbol{m} = \rho \boldsymbol{u}$; and pressure, p) are expanded in terms of a Fourier representation in the horizontal directions and a third-order (quadratic) B-spline representation in the wall-normal direction. The Fourier directions are de-aliased using the 3/2-rule, where all nonlinear terms are calculated using 3/2 times the number of modes used to advance the solution. Quadratic nonlinearities are fully de-aliased using this rule while higher-order nonlinearities are only partially de-aliased. B-splines have a variety of good numerical properties, and have been used successfully in the incompressible pipe flow simulation of Loulou (1996) and the compressible jet of Rao (1997). B-splines have high resolving power, allow easy implementation of boundary conditions, and allow the use of stretched grids. More details on B-splines may be found in: De Boor (1978), Kravchenko, Moin & Moser (1996), and Shariff & Moser (1998). Their use in the present work is described in Guarini (1998). In the wall-normal direction, Giles' (1989, 1990) second-order non-reflecting boundary conditions are used at the free-stream boundary and adiabatic no-slip boundary conditions are used at the wall. This combination of splines and Fourier methods produces a very accurate numerical method. For the time discretization the mixed implicit/explicit method of Spalart, Moser & Rogers (1991) is used. All terms are

Sim.	M	Re_θ	$N_x \times N_z$	$L_x^+ \times L_z^+$	$\Delta x^+ \times \Delta z^+$
S1	0.0	225	—	—	—
S2	0.0	300	85×64	$2680^+ \times 670^+$	$31.5^+ \times 10.5^+$
S3	0.0	670	171×128	$4900^+ \times 1225^+$	$28.7^+ \times 9.50^+$
S4	0.0	1410	288×213	$11400^+ \times 2850^+$	$39.6^+ \times 13.4^+$
KMM	0.0	—	192×160	$2300^+ \times 1150^+$	$12.0^+ \times 7.00^+$
GA	3.0	3015	192×144	$527^+ \times 300^+$	$2.74^+ \times 2.08^+$
GA	4.5	2618	180×144	$260^+ \times 155^+$	$1.44^+ \times 1.08^+$
GA	6.0	2652	180×128	$229^+ \times 137^+$	$1.27^+ \times 1.07^+$
Rai	2.25	6000	971×321	full spatial	$27.0^+ \times 10.4^+$
Present	2.5	1577	256×192	$2269^+ \times 1134^+$	$8.86^+ \times 5.91^+$

TABLE 1. Comparison of parameters used in the incompressible simulations of Spalart (1988) (S1–S4) and Kim *et al.* (1987) (KMM); the compressible simulations of Guo & Adams (1994) (GA) and Rai *et al.* (1995); and the present simulation.

treated explicitly except for the highest wall-normal derivative in the viscous, pressure gradient, and 'acoustic coupling term'

$$\gamma \sigma p \frac{\partial m_2}{\partial x_2}, \tag{2.1}$$

that appears in the pressure equation. In the implicit treatment, non-constant coefficients that vary in the horizontal directions cannot be easily treated. Both the viscous and acoustic coupling terms are split into a term with coefficients (viscosity and σp respectively) varying in the wall-normal direction only, which is treated implicitly, and the remainder, which is treated explicitly.

2.2. *Choice of parameters*

A turbulent boundary layer at a Mach number of 2.5 and a Reynolds number based on displacement thickness of $Re_{\delta^*} = 6258$ was simulated. This results in a Reynolds number based on momentum integral thickness and wall viscosity of $Re_{\theta'} \approx 849$. The Reynolds number based on momentum integral thickness and free-stream viscosity was $Re_\theta \approx 1577$. The Mach number was chosen because of the availability of experimental data and because it is in a range where we might begin to see some compressibility effects.

There are two important sets of parameters, the grid size ($N_x \times N_y \times N_z$) and the domain size ($L_x \times L_y \times L_z$), that determine the overall quality/accuracy of the simulation. The coordinate system is oriented such that the x-, y-, and z-directions are the streamwise, wall-normal, and spanwise directions, respectively (in this paper we use a mixed index or symbol notation where x_1, x_2, and x_3 correspond to x, y, and z, respectively). The current simulation has $256 \times 209 \times 192$ ($N_x \times N_y \times N_z$) Fourier–B-spline modes and a domain size of $2269^+ \times 875^+ \times 1134^+$ ($L_x \times L_y \times L_z$), where $y^+ = y u_\tau / \nu_w$. Here ν_w is the kinematic viscosity at the wall and u_τ is the friction velocity $(\tau_w/\rho_w)^{1/2}$, where τ_w and ρ_w are the shear stress and density at the wall, respectively. The domain and grid parameters were selected to provide sufficient resolution in a domain that is large enough to eliminate most finite domain size effects. That this is the case is demonstrated below.

One way to assess the adequacy of the resolution and domain size is by comparison to DNS of similar flows. The resolution and domain size used in the current simulation

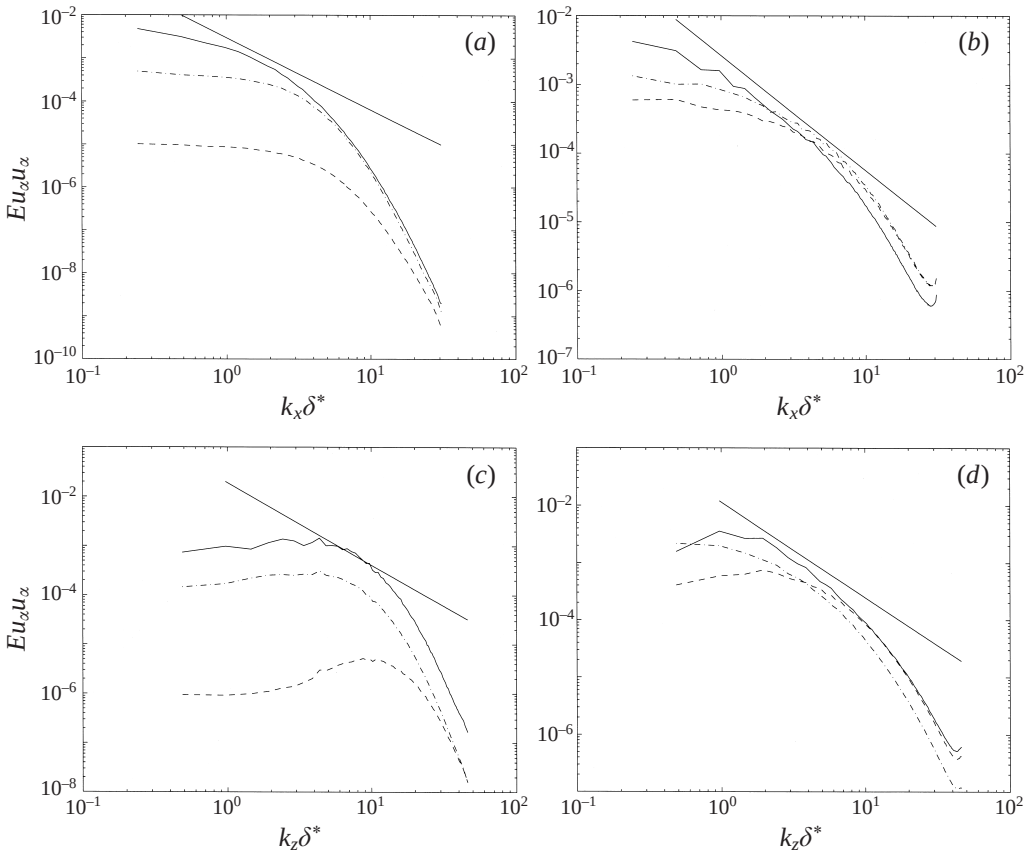

FIGURE 1. One dimensional energy spectra $E_{u_\alpha u_\alpha}$. Plotted versus (*a*) k_x at $y^+ = 4$; (*b*) k_x at $y^+ = 80$; (*c*) k_z at $y^+ = 4$; (*d*) k_z at $y^+ = 80$. ———, Streamwise velocity component; – – – –, wall-normal velocity component; —·—, spanwise velocity component.

are compared with the incompressible boundary layer simulations of Spalart (1988) (S1–S4), the incompressible channel flow of Kim *et al.* (1987) (KMM) and the compressible boundary layer simulations of Guo & Adams (1994) (GA) (table 1). The resolution required in the $M = 3$ simulation of Guo & Adams was significantly finer than that of the incompressible simulations or the present simulation. The reason for Guo & Adams' extremely fine resolution is not clear. However, the need for increased resolution of the current simulation relative to KMM is due to sharp density gradients present in the compressible flow. KMM is used for comparison because their resolution is better than Spalart's simulations, as determined by the drop in energy spectra. The adequacy of the spatial resolution was confirmed by examining the spectra, where $E_{u_\alpha u_\alpha}$ is the energy spectrum for the velocity component u_i. Examples are shown in figure 1. These spectra and those at other y-locations suggest the resolution is adequate. Another indication of the adequacy of the resolution is the value of $k_{max}\eta$, where k_{max} is the maximum wavenumber in x and η is the local Kolmogorov scale. The maximum and minimum of this value in the current simulation are 1.6 and 0.5, respectively, which is considered adequate. For comparison the simulation of Kim *et al.* (1987) had values of 1 and 0.4 for the maximum and minimum, respectively.

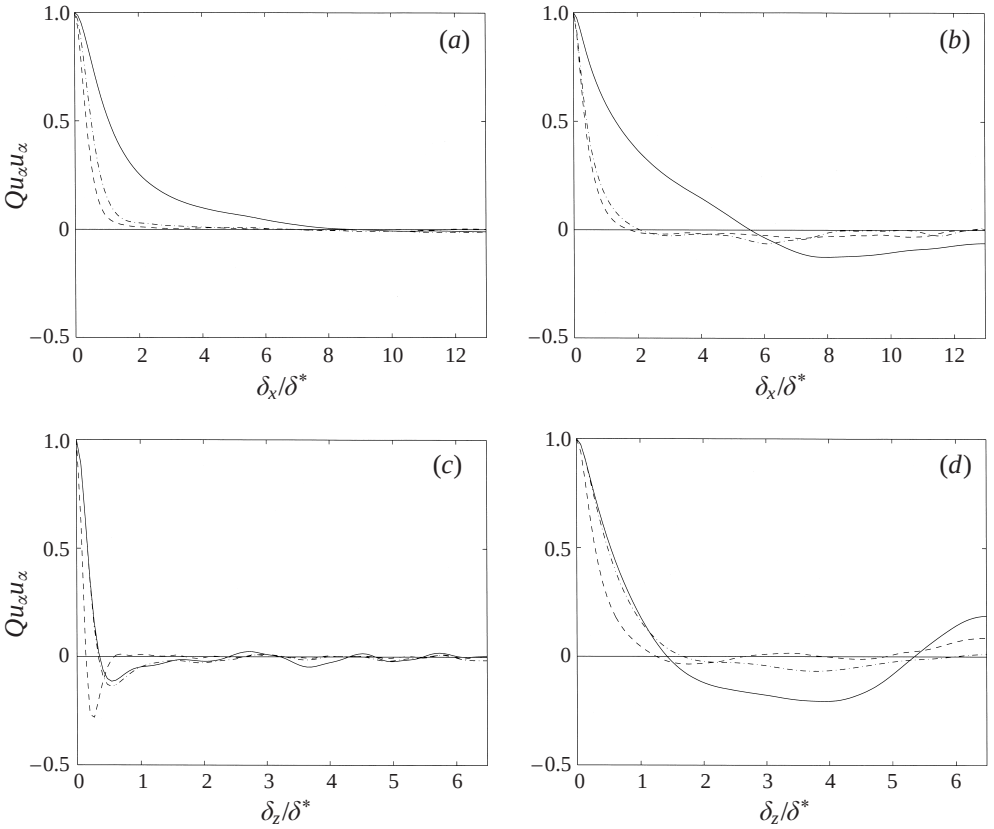

FIGURE 2. Two-point correlations $Q_{u_\alpha u_\alpha}$. Plotted versus (*a*) δ_x/δ^* at $y^+ = 4$; (*b*) δ_x/δ^* at $y^+ = 150$; (*c*) δ_z/δ^* at $y^+ = 4$; (*d*) δ_z/δ^* at $y^+ = 150$. ———, Streamwise velocity component; – – – –, wall-normal velocity component; —·—, spanwise velocity component.

The periodic domain size of the current simulation was selected to ensure that the streamwise and spanwise two-point correlations are nearly zero for large separations, where the two-point correlation for the velocity component u_i is $Q_{u_\alpha u_\alpha}$. As is evident in figure 2, the near-wall correlations are indeed near zero for large separations, though they could be better for the streamwise component. However, far from the wall ($y^+ = 150$) low-level large-scale coherence is evident in the correlation, perhaps due to acoustics as suggested by Coleman, Kim & Moser (1995).

In the wall-normal direction, the B-splines were defined on a non-uniform set of knots (grid points) which is given by

$$t_i = (\Delta y_{max} - \Delta y_{min}) \left[\frac{\mathrm{i}N_m}{N_k} + (\mathrm{e}^{-\alpha \mathrm{i}N_m/N_k} - 1)/\alpha \right] + \frac{\Delta y_{min} \mathrm{i}N_m}{N_k}, \tag{2.2}$$

where $\alpha = 0.14$, $N_m = 1.09$, $N_k = 207$, $\Delta y_{min} = 1.0$, and $\Delta y_{max} = 110.0$. With this distribution there were 13 grid points in the first 9 wall units, including the grid point at the wall. The minimum grid spacing in the wall-normal direction was 0.48^+ wall units while the maximum was 7.8^+ wall units at the free-stream boundary, which was located at $y^+ = 875$.

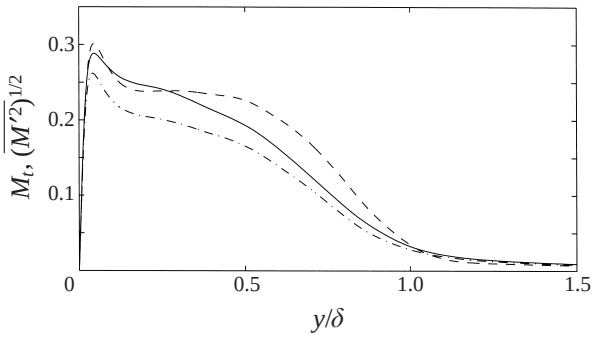

FIGURE 3. Turbulent and fluctuating Mach numbers as functions of y/δ: ———, turbulent Mach number, M_t; – – – –, RMS of Mach number fluctuations, $(\overline{M'^2})^{1/2}$; —·—, turbulent Mach number with spanwise component removed.

2.3. *A note on averaging*

In the results that follow, both Reynolds and Favre averaging are used depending on simplicity of presentation and conventions used in the papers to which we are comparing. In each case care will be taken to distinguish between the two.

The Reynolds average of f over the x- and z-directions will be denoted by $\bar{f}$, and fluctuations about this mean will be denoted by f'. The Favre average over the x- and z-directions, $\tilde{f}$, is a density-weighted average:

$$\tilde{f} = \frac{\overline{\rho f}}{\bar{\rho}}. \tag{2.3}$$

Fluctuations about the Favre average will be denoted by f''.

2.4. *The turbulent Mach number*

One convenient measure of the turbulent compressibility effects is the fluctuating Mach number, M', which is just the RMS fluctuation of the Mach number. A similar quantity is the turbulent Mach number given by

$$M_t = \frac{(\overline{u_i' u_i'})^{1/2}}{\bar{a}}. \tag{2.4}$$

Morkovin (1962) suggests that the turbulence is only weakly affected by compressibility provided $M' \lesssim 0.2$ (0.3 according to Spina *et al.* 1994). Despite the relatively low Mach number, the peak values of M' and M_t in the simulation are approximately 0.3 (figure 3). Nevertheless, as will be shown in § 3, Morkovin's density scaling and the Van Driest transformation still apply. The shoulder in figure 3 is at $(\overline{M'^2})^{1/2} \approx 0.25$, while the experimental data shown in Spina *et al.* (1994), for $M_\infty = 2.3$ and $Re_\theta = 4700$, have a shoulder at $(\overline{M'^2})^{1/2} \approx 0.20$. The reason for the difference is most likely the neglect, in the experiments, of the spanwise velocity in calculating the Mach number. As one can see in figure 3, the turbulent Mach number is consistent with the experimental value of 0.2 when the spanwise velocity component is not included.

A measure of intrinsic compressibility is the ratio of mean-square dilatation fluctuations to mean-square vorticity fluctuations:

$$\overline{(\partial u_i'/\partial x_i)(\partial u_j'/\partial x_j)}/\overline{\omega_k' \omega_k'}. \tag{2.5}$$

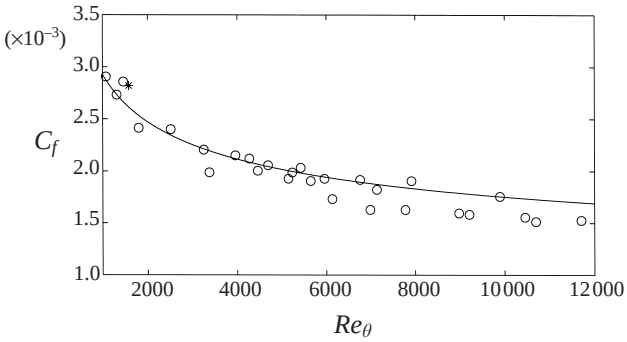

FIGURE 4. Comparison of the computational C_f with the experimental data of Coles (1954): ∗, simulation data point; ○, experimental data points ($2.2 \leqslant M \leqslant 2.8$); ———, Van Driest II (Bardina *et al.* 1997).

This ratio measures the level of compressibility, as given by dilatation, relative to the turbulent motion, as given by enstrophy. In the simulation we find that this ratio is approximately 5×10^{-4} throughout the boundary layer.

3. Turbulence statistics

In this section, several turbulence statistics are examined to evaluate their consistency with accepted experimental and computational results.

To obtain statistics, averages are computed over the streamwise and spanwise directions of each field; then an ensemble average over 55 fields spanning 31.33 time units was calculated. Time is non-dimensionalized by δ^*/a_∞. The flow was determined to be stationary when several quantities (C_f, θ, u_τ, Re'_θ, and T_w) began to oscillate about a mean value.

3.1. *Mean flow*

The skin friction coefficient is defined as

$$C_f = 2\left(\frac{u_\tau}{U_\infty}\right)^2 \frac{\bar{\rho}_w}{\bar{\rho}_\infty}. \tag{3.1}$$

In the simulation the skin friction coefficient was found to be $C_f \approx 0.00282$. There are very few experimental studies at the low Reynolds number of the simulation. However, the simulation compares favourably with the experimental results compiled by Coles (1954) and the skin friction correlation given in Bardina, Huang & Coakley (1997) based on the Van Driest II skin friction transformation (figure 4).

The Van Driest transformed velocity, U_c, is plotted in wall units in figure 5. U_c is defined as

$$U_c = \int_0^U (\overline{T}_w/\overline{T})^{1/2}\,\mathrm{d}U. \tag{3.2}$$

Experiments have shown that U_c satisfies the same scaling laws as the mean streamwise velocity in incompressible flow. On the plot we have included the linear sub-layer relation, $U_c^+ = y^+$, the standard log-law, and a composite profile that consists of Reichardt's (1951) inner layer profile and Finley's wake function (Cebeci & Bradshaw

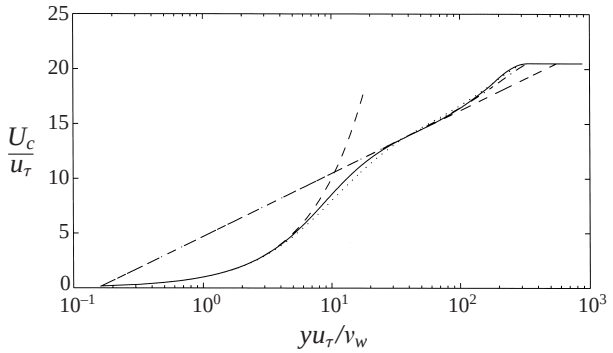

FIGURE 5. Van Driest transformed velocity in wall units: ———, DNS time average; – – – –, linear sub-layer $U_c^+ = y^+$; – – – –, log-law $U_c^+ = (1/0.40)\ln(yu_\tau/\nu_w) + 4.7$; ·····, Reichardt's profile with Finley's wake function; —·—, Coles' profile.

1977):

$$\frac{U_c}{u_\tau} = \frac{1}{\kappa}\ln\left(1+\kappa\frac{yu_\tau}{\nu_w}\right) + C_1\left[1 - \mathrm{e}^{-yu_\tau/(\eta_1\nu_w)} - \left(\frac{yu_\tau}{\eta_1\nu_w}\right)\mathrm{e}^{-yu_\tau b/(\nu_w)}\right] + \frac{1}{\kappa}\left[\left(\frac{y}{\delta}\right)^2 - \left(\frac{y}{\delta}\right)^3 + 6\Pi\left(\frac{y}{\delta}\right)^2 - 4\Pi\left(\frac{y}{\delta}\right)^3\right], \quad (3.3)$$

where δ is the y location at which $U_c(y=\delta) = U_{c_\infty}$, $C_1 = -(1/\kappa)\ln(\kappa) + C$, $\eta_1 = 11$, and $b = 0.33$. This profile is used in the Appendix to calculate the slow-growth terms. In addition, the more commonly cited Coles' profile (Coles 1956) is shown. In the region of $30 \leqslant y^+ \leqslant 70$, the simulation data fall on the log-law curve, where we have chosen the constants $\kappa = 0.40$ and $C = 4.7$ for the plot; κ was determined by finding the minimum of $y^+(\partial U_c^+/\partial y^+)$ as a function of y^+. Using this value and the location of the minimum, C was then calculated. These values compare well with those of Spalart (1988), and κ is within the range of values quoted in the literature (see Smits & Dussauge 1996). At low Reynolds numbers the log-region becomes vanishingly thin making the determination of κ and C difficult. There is also some disagreement as to whether or not the values are Reynolds number dependent at the low Reynolds number of the simulation (Spalart 1988). The value of Π for the time-averaged profile was $\Pi = 0.25$, determined from the equations in the Appendix. Reichardt's 'basic' profile with Finley's wake function gives a rather good representation of U_c throughout the boundary layer. Since this is the profile shape assumed when computing the slow streamwise derivatives (see the Appendix), the good agreement implies that the assumed profile does not introduce a significant error in the computation of these derivatives. It is interesting to note that if we use U rather than the transformed velocity U_c the values of κ and C are 0.477 and 2.64, respectively, which are quite different from the incompressible values.

3.2. *RMS velocity, pressure, and vorticity*

When normalized by u_τ the turbulence intensities from the current compressible boundary layer are lower than the intensities from the incompressible boundary layer (figure 6*a*). Morkovin (1962) predicted that scaling by the square root of the mean density profile should collapse RMS data for the streamwise velocity component and possibly the spanwise and wall-normal components. When this scaling

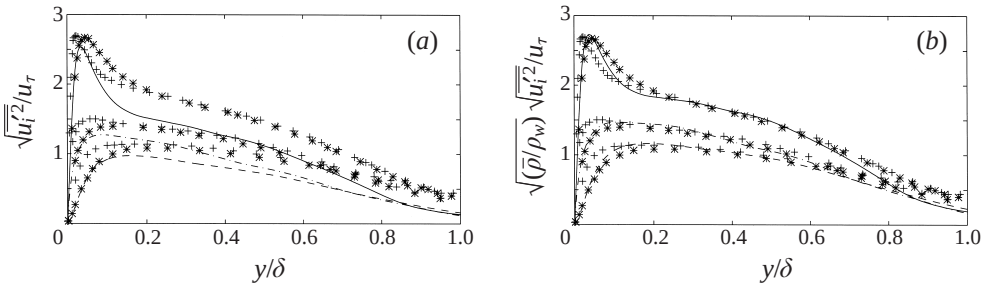

FIGURE 6. RMS velocity profiles plotted versus y/δ, (*a*) scaled by $1/u_\tau$, and (*b*) scaled by $\sqrt{(\bar{\rho}/\rho_w)}/u_\tau$. Lines correspond to the compressible simulation and symbols are used for Spalart's incompressible simulations: ———, streamwise velocity component; – – – –, wall-normal velocity component; —·—, spanwise velocity component; +, Spalart ($Re_\theta = 1410$); *, Spalart ($Re_\theta = 670$).

is used there is good agreement for all three velocity components (figure 6*b*). In the experiments good collapse is obtained for the streamwise component but the experiments are inconclusive with respect to the collapse of the other two components (Smits & Dussauge 1996). Smits & Dussauge (1996) attribute this to both the difficulty in measuring the spanwise and wall-normal components and the scarcity of measurements of these two components.

There are two additional points which need to be mentioned in connection with figure 6. The first is that Re_θ, based on local viscosity in the compressible simulation, varies across the boundary layer from 849 to 1577. Spalart's (1988) two simulations at $Re_\theta = 670$ and 1410 span this range. This is important because in y/δ units, the location of the peaks in the intensities moves toward the wall, since it remains approximately fixed in wall units. Further, Spalart showed that at these low Reynolds numbers, the magnitude of the peaks in intensities increases with Reynolds number. The second issue concerns the choice of δ in figure 6. As discussed by Spalart, the collapse of the data over a wide range of Reynolds numbers is sensitive to the choice of δ. In making our comparison, we used a definition of δ based on the composite profile of (3.3) and made no effort to find a definition that would better collapse the data. This might account for the differences that are evident at $y \geqslant 0.65\delta$.

In the compressible simulation the pressure fluctuations, when scaled by $\rho_w u_\tau^2$, are larger than those found in the incompressible simulations through most of the boundary layer (figure 7). The peak pressure fluctuations are larger than Spalart's $Re_\theta = 670$ simulation and occur at nearly the same location. The value of the RMS pressure at the wall and at the peak are $(p'_{rms})_w/(\rho_w u_\tau^2) \approx 2.7$ and $(p'_{rms})_{max}/(\rho_w u_\tau^2) \approx 3.0$, respectively. In the free stream the pressure fluctuations approach $(p'_{rms})_\infty/(\rho_w u_\tau^2) \approx 0.47$. This is comparable to the value of the radiated pressure measured by Laufer (1964) of $(p'_{rms})_\infty/(\rho_w u_\tau^2) \approx 0.4$.

RMS vorticity profiles for the present simulation agree very well with those found in Spalart's incompressible simulations when normalized by u_τ^2/ν_w (figure 8) and plotted in wall units, with the compressible results being slightly larger than the incompressible simulations away from the wall. Note that from Spalart's data it is clear that near the wall the maximum may be Reynolds number dependent. The near-wall RMS vorticity is shown plotted in wall units here because the wall scaling is known to (approximately) collapse such profiles for different Reynolds numbers in incompressible flows, and indeed in y/δ units our data did not collapse with that of Spalart's.

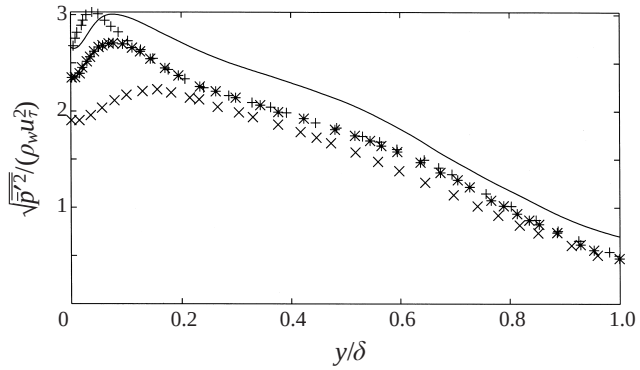

FIGURE 7. RMS pressure fluctuations versus y/δ: ———, compressible DNS; +, Spalart ($Re_\theta = 1410$); *, Spalart ($Re_\theta = 670$); ×, Spalart ($Re_\theta = 300$).

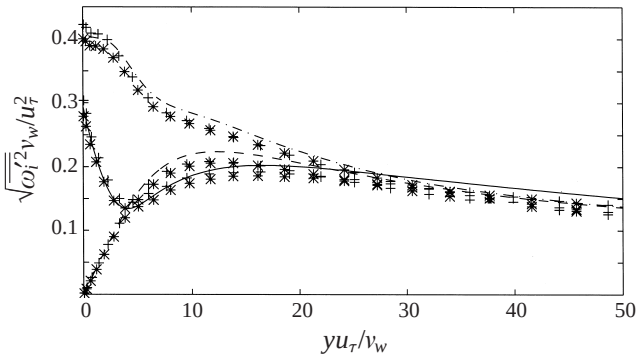

FIGURE 8. RMS of vorticity fluctuations. Lines correspond to the compressible simulation: ———, $\overline{\omega_1'^2}$; – – – –, $\overline{\omega_2'^2}$; —·—, $\overline{\omega_3'^2}$; +, Spalart ($Re_\theta = 1410$); *, Spalart ($Re_\theta = 670$).

3.3. *Reynolds shear stress*

Reynolds averaging the momentum equation,

$$\frac{\partial \rho u_i}{\partial t} = -\frac{\partial}{\partial x_j}\{\rho u_i u_j\} - \frac{\partial p}{\partial x_i} + \frac{1}{Re}\frac{\partial \tau_{ij}}{\partial x_j}, \tag{3.4}$$

we get

$$\frac{\partial \bar{\rho}\tilde{u}_i}{\partial t} = -\frac{\partial}{\partial x_j}\{\bar{\rho}\tilde{u}_i\tilde{u}_j + \overline{\rho u_i'' u_j''}\} - \frac{\partial \bar{p}}{\partial x_i} + \frac{1}{Re}\frac{\partial \bar{\tau}_{ij}}{\partial x_j}. \tag{3.5}$$

The sum of the Reynolds shear stress and mean shear stress terms is

$$\frac{\partial}{\partial x_2}\left\{-\overline{\rho u_i'' u_2''} + \frac{1}{Re}\left[\bar{\mu}\frac{\partial \bar{u}_1}{\partial x_2} + \overline{\mu'\left(\frac{\partial u_1'}{\partial x_2} + \frac{\partial u_2'}{\partial x_1}\right)}\right]\right\}. \tag{3.6}$$

In incompressible boundary layers a constant total stress region is observed near the wall. The constant-stress region is consistent with the law of the wall and is also present in the current simulation (figure 9). The constant-stress region extends to 30 or 40 wall units above the wall.

As was the case for the turbulence intensities, $\overline{u'v'}$ agrees with the incompressible

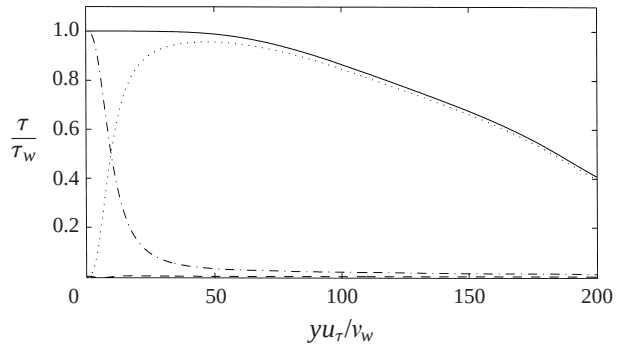

FIGURE 9. Simulation results for Reynolds stress, mean shear stress, and total stress versus yu_τ/ν_w: ———, total shear stress; ·····, Reynolds stress ($\overline{\rho u_1'' u_2''}$); —·—, mean shear stress ($\overline{\mu}(\partial\overline{u}/\partial y)$); – – – –, stress correlations ($\overline{\mu'[(\partial u'/\partial y)+(\partial v'/\partial x)]}$).

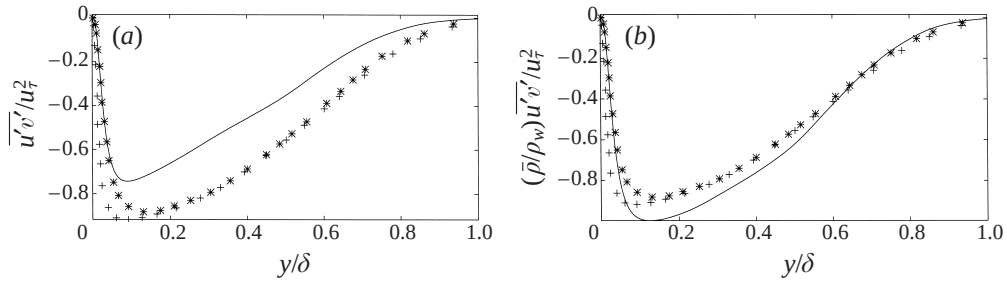

FIGURE 10. $\overline{u'v'}$ versus y/δ, (*a*) scaled by $1/u_\tau^2$, and (*b*) scaled by $(\overline{\rho}/\rho_w)/u_\tau^2$: ———, compressible DNS; +, Spalart ($Re_\theta = 1410$); *, Spalart ($Re_\theta = 670$).

results when scaled by the local mean density (figure 10). This agreement is not as close as for the intensities, but this is primarily due to the square root in the definition of the intensities.

4. Reynolds analogies

For incompressible laminar boundary layers, the similarity of the momentum and energy equations allows one to approximately relate quantities pertaining to heat transfer with quantities pertaining to momentum transfer. O. Reynolds discovered this principle in its simplest form. The 'Reynolds analogy' has been extended with additional approximations to the compressible and turbulent cases. Morkovin (1962) suggests that a Reynolds analogy might apply to compressible turbulence, a concept known as the 'strong Reynolds analogy (SRA)'. More recently, other expressions of a Reynolds analogy have been formulated by several authors (Gaviglio 1987 and Huang, Coleman & Bradshaw 1995), and these will also be studied below.

4.1. *The strong Reynolds analogy*

To investigate the validity of the strong Reynolds analogy, and its consequences, a brief review of its derivation and a critical examination of the underlying assumptions are given in this section. The analogy is based on the observation that the transport equations for mean velocity and mean total enthalpy, $h_t = C_p T + u_i^2/2$, for a stationary,

zero-pressure-gradient boundary layer,

$$\bar{\rho}\tilde{u}_1\frac{\partial\tilde{u}_1}{\partial x_1}+\bar{\rho}\tilde{u}_2\frac{\partial\tilde{u}_1}{\partial x_2}=\frac{\partial}{\partial x_2}\left\{\bar{\mu}\frac{\partial\tilde{u}_1}{\partial x_2}-\overline{\rho u_1''u_2''}\right\}, \tag{4.1a}$$

$$\bar{\rho}\tilde{u}_1\frac{\partial\tilde{h}_t}{\partial x_1}+\bar{\rho}\tilde{u}_2\frac{\partial\tilde{h}_t}{\partial x_2}=\frac{\partial}{\partial x_2}\left\{\frac{\bar{\mu}}{Pr}\frac{\partial\tilde{h}_t}{\partial x_2}-\overline{\rho u_2''h_t''}\right\}, \tag{4.1b}$$

have the same form if the Prandtl number is 1. If the Prandtl numbers are different, the equations are still of the same form provided the molecular diffusivity can be neglected, which is true in a turbulent boundary layer, except very near the wall. The two equations, however, have different boundary conditions.

The total temperature, T_t, is defined by the relationship $h_t = C_p T_t$. If one assumes that gradients of mean total temperature and velocity in x can be neglected and further (without justification) that

$$T_t'' = Cu_1'', \tag{4.2}$$

one can eliminate the turbulent terms in the mean transport equations and solve for $\tilde{T}_t$ in terms of $\tilde{u}_1$,

$$\tilde{T}_t = C\tilde{u}_1 + D. \tag{4.3}$$

This result was first stated in a slightly different form by Young (1953)† and later by Morkovin (1962), who called assumption (4.2) the strong Reynolds analogy. Since $\partial\tilde{T}_t/\partial y = 0$ at an adiabatic wall and the velocity gradient, $\partial\tilde{u}_1/\partial y$, is non-zero at the wall, it follows that the constant, C, must be zero. This implies that the mean total temperature is constant with value $\tilde{T}_{tw}$ and the total temperature fluctuations are zero. In the current simulation the maximum deviation of the mean total temperature from a constant is about 7%, thus approximately verifying the result for the mean. However, in the simulation, RMS total temperature fluctuations are comparable in magnitude to the static temperature fluctuations (see figure 11), and are thus not negligible. The discussion that follows addresses the validity of (4.2), with $C = 0$, and the relationships derived from it.

The fact that measured total temperature fluctuations are not negligible was recognized by Morkovin (1962). Nonetheless, relations derived assuming that they are negligible have been widely used in the literature. These relations can be obtained by writing the definition of total temperature and subtracting its Favre mean:

$$C_p T_t'' = C_p T'' + \tilde{u}_i u_i'' + \frac{u_i'' u_i''}{2} - \widetilde{\frac{u_i'' u_i''}{2}}. \tag{4.4}$$

By retaining only the terms that are linear in the fluctuations, and assuming that $\tilde{u}_1 u_1'' \gg \tilde{u}_2 u_2''$ and $\tilde{u}_1 u_1'' \gg \tilde{u}_3 u_3''$, we get

$$C_p T_t'' = C_p T'' + \tilde{u}_1 u_1''. \tag{4.5}$$

So far, the approximations made are excellent. One can verify this by considering the correlation coefficient $R_{u_1''(T_t''-T'')}$ between streamwise velocity fluctuations and the difference between total and static temperature fluctuations. The correlation coefficient differs from unity by less than 0.9% for $y/\delta > 0.05$, showing that (4.5) is very accurate.

In Morkovin's analysis, the SRA is invoked to argue that the total temperature

† Young calls (4.3) and (4.2) solutions to the equations. This terminology is imprecise and attaches too much legitimacy to (4.3) and (4.2). We prefer not to identify the two as solutions, but rather to say that the assumption (4.2) implies (4.3).

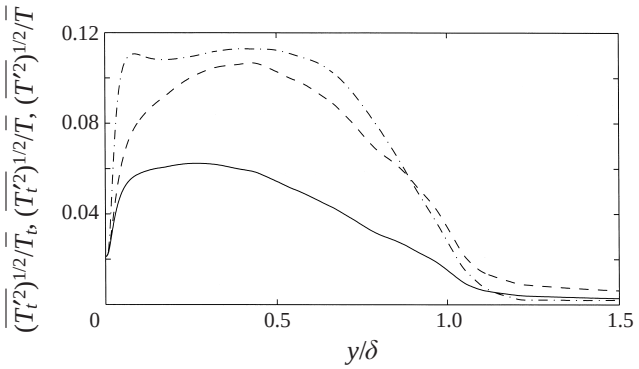

FIGURE 11. Comparison of RMS total and static temperature fluctuations: ———, $(\overline{T_t'^2})^{1/2}/\overline{T}_t$; – – – –, $(\overline{T_t'^2})^{1/2}/\overline{T}$; —·—, $(\overline{T'^2})^{1/2}/\overline{T}$.

fluctuations are negligible compared to the static temperature fluctuations, and thus (4.5) becomes

$$C_p T'' + \tilde{u}_1 u_1'' \approx 0, \tag{4.6}$$

which is not valid, as discussed above (figure 11). Substituting $\gamma R/(\gamma - 1)$ for C_p and defining the Mach number, M_a:

$$M_a^2 = \frac{\tilde{u}_1^2}{\gamma R \tilde{T}}, \tag{4.7}$$

(4.6) can be rewritten:

$$\frac{T''}{\tilde{T}} = -(\gamma - 1) M_a^2 \frac{u_1''}{\tilde{u}_1}. \tag{4.8}$$

The (questionable) relations, (4.6) and (4.8), between T'' and u_1'' have several statistical consequences which are given by

$$\frac{(\overline{T''^2})^{1/2}/\tilde{T}}{(\gamma - 1) M_a^2 (\overline{u''^2})^{1/2}/\tilde{u}} \approx 1, \tag{4.9a}$$

$$-R_{u_1'' T''} \approx 1, \tag{4.9b}$$

$$Pr_t = \frac{\overline{\rho u_1'' u_2''}(\partial \tilde{T}/\partial y)}{\overline{\rho u_2'' T''}(\partial \tilde{u}_1/\partial y)} \approx 1. \tag{4.9c}$$

These are three of the five SRA relationships Morkovin (1962) presented. Equations (4.9*a*) and (4.9*b*) are direct consequences of (4.6), whereas (4.9*c*) is obtained by multiplying (4.6) by $\rho u_2''$, averaging, and assuming that

$$\tilde{u}_1 = -C_p \left(\frac{\partial \tilde{T}}{\partial y} \right) \Bigg/ \left(\frac{\partial \tilde{u}_1}{\partial y} \right), \tag{4.10}$$

which comes from the mean total temperature equation when it is assumed that $\tilde{T}_t$ is constant and that nonlinear fluctuating terms and velocity components other than $\tilde{u}_1$ are small.

From the simulation results we see that equation (4.9*a*) is satisfied for $y/\delta < 0.6$ (figure 12). However, in the same region, (4.9*b*) and (4.9*c*) are not satisfied (see figures 13 and 14). The correlation $R_{u_1'' T''}$ is approximately 0.6 through most of the boundary

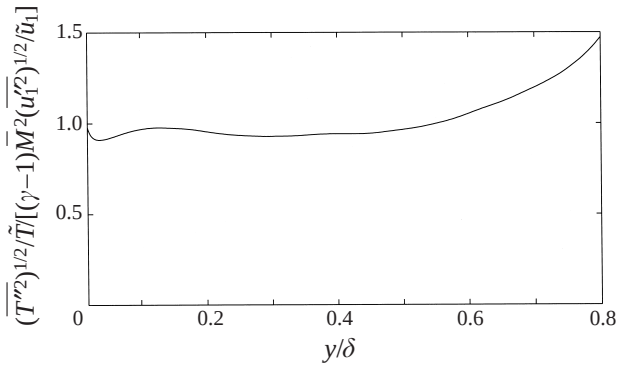

FIGURE 12. Test of the strong Reynolds analogy, as expressed by (4.9*a*).

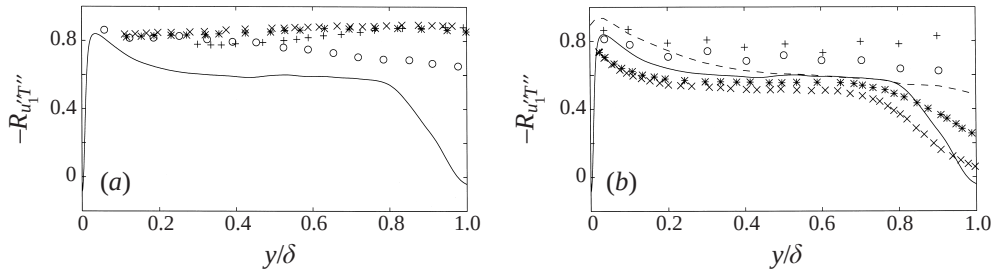

FIGURE 13. Correlation coefficient, $-R_{u_1''T''}$, versus y/δ. (*a*) Comparison with compressible experiments: ———, time average of DNS; ×, Debieve ($M = 2.3$, $Re_\theta = 5650$) (Gaviglio 1987); ∗, Debieve ($M = 2.3$, $Re_\theta = 5650$) (Gaviglio 1987); +, Dussauge ($M = 1.7$, $Re_\theta = 5700$) (Gaviglio 1987); ○, Smith & Smits (1993) ($M = 2.9$, $Re_\theta = 77\,600$). (*b*) Comparison with incompressible experiments: ———, time average of DNS; ×, Fulachier ($Re_\theta = 5000$) (Gaviglio 1987); ∗, Rey (Gaviglio 1987); +, Subramanian & Antonia (1981) $Re_\theta = 990$; ○, Subramanian & Antonia (1981) $Re_\theta = 7100$; – – – –, incompressible simulation of Bell & Ferziger (1993).

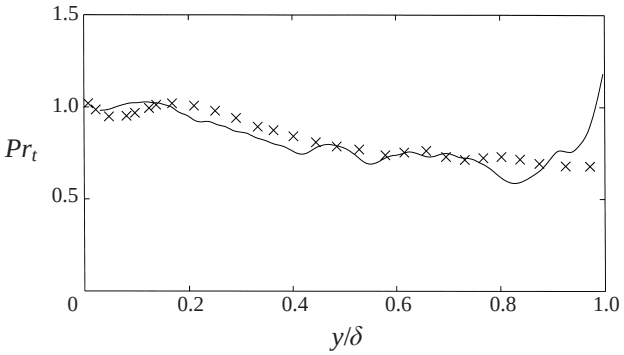

FIGURE 14. Turbulent Prandtl number, Pr_t, versus y/δ: ———, time average DNS data; ×, incompressible heated wall simulations of Bell & Ferziger (1993).

layer, and the turbulent Prandtl number is about 0.7 except near the wall ($y/\delta < 0.2$) where it is near 1. The current results for the velocity–temperature correlation are in disagreement with the available data from compressible boundary layer experiments (figure 13), which show the correlation to be close to 1 (approximately 0.9), in agreement with predictions of the SRA.

The reason for this disagreement between simulations and experiments is not clear, but is of great interest. The speculations of Gaviglio (1987) that the large correlation values observed in experiments are due to acoustic waves suggests the possibility that the acoustics are somehow different (weaker) in the simulations. However, tests for numerical artifacts (e.g. damping) in the simulated acoustics did not reveal any problems, and our radiated sound pressure magnitude compares well with that of Laufer (1964). Another interesting observation is that in the current simulations both the velocity–temperature correlations and the turbulent Prandtl number agree reasonably well with data from incompressible boundary layers, both experimental and computational (see figures 13*b* and 14). This might be expected, given the weak compressibility of the boundary layer at this Mach number. This agreement at least makes plausible the proposition that the current simulation results are physical, despite disagreement with compressible experiments. The basis for comparison with the incompressible heated wall in figure 13(*b*) is that the heated wall produces a temperature gradient of the same sign as that obtained in the current simulation.

Further analysis suggests that the key to the discrepancy is the magnitude of the total temperature fluctuations. In the experiments, it is total temperature and momentum that are measured directly, with other quantities computed using several approximate relations. By using these relations in the simulation data it was found that (*a*) they yield accurate values for the derived quantities; and (*b*) when the total temperature fluctuations in the simulations are reduced by a factor of 2, the relations used in the experiments yield correlations $R_{u_1'' T''}$ consistent with the experiments. The total temperature fluctuations in the experiments are indeed approximately a factor of 2 lower than the simulations (Kistler 1959). A factor of 2 error in the total temperature is much larger than the uncertainties in either the experiments or the simulation, so there is clearly something wrong with one or the other (or both). A potentially useful approach to settling this question would be to use a physical model of the experimental probes in the simulations, and process the resulting signals as is done in the experiments, to see if results consistent with the experiments are recovered. Until this issue is resolved, it would be wise to view both the experimental and computational results on these quantities with some suspicion.

Of the three relations shown, only the RMS relation (4.9*a*) is very nearly satisfied. The question arises as to how this relationship can be satisfied even though total temperature fluctuations are of the same order as temperature fluctuations. This success of (4.9*a*) can be explained by rearranging the definition of total temperature fluctuations (4.5) as follows:

$$\frac{\overline{T''^2} + \overline{T_t''^2} - 2\overline{T_t'' T''}}{\tilde{T}^2} = (\gamma - 1)^2 M_a^4 \frac{\overline{u_1''^2}}{\tilde{u}_1^2}. \tag{4.11}$$

The condition that must be satisfied for (4.9*a*) to be valid when total temperature fluctuations are not neglected is

$$\frac{\overline{T''^2}}{\tilde{T}^2} \gg \frac{\overline{T_t''^2} - 2\overline{T_t'' T''}}{\tilde{T}^2}, \tag{4.12}$$

which the simulation data confirms (figure 15). While all the terms on the left-hand side of (4.11) are of the same order, in the inner portion of the boundary layer the term on the left-hand side of (4.12) is nearly a factor of 6 greater than the term on the right. So the success of (4.9*a*) is due to a relationship between total and static

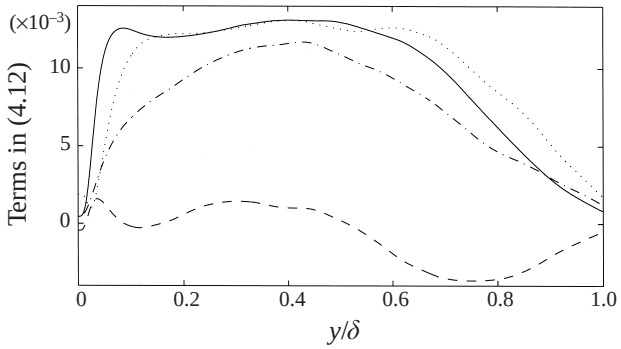

FIGURE 15. Comparison of terms in (4.12): ———, $\overline{T''^2}/\tilde{T}^2$; —·—, $\overline{T_t''^2}/\tilde{T}^2$; ·····, $-2\overline{T_t'' T''}/\tilde{T}^2$; – – – –, $(\overline{T_t''^2} - 2\overline{T_t'' T''})/\tilde{T}^2$.

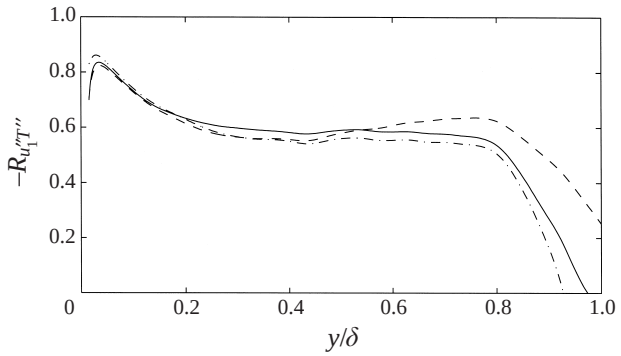

FIGURE 16. Comparison of $R_{u_1''T''}$ from (4.15) to simulation data: ———, time average of DNS data; – – – –, profile predicted by (4.15); —·—, profile predicted by the modified Reynolds analogy of Huang *et al.* (1995).

temperature fluctuations rather than the assumption of negligible total temperature fluctuations.

Gaviglio (1987) has shown that fluctuations in total and static temperature can be directly related to the correlation coefficient $R_{u_1''T''}$ if (4.9*a*) is assumed to be valid. The RMS of the linearized definition of total temperature, (4.5), is

$$(\overline{T_t''^2})^{1/2} = \left(\overline{T''^2} + \frac{\tilde{u}_1^2}{C_p^2}\overline{u_1''^2} + 2\frac{\tilde{u}_1}{C_p}(\overline{T''^2})^{1/2}(\overline{u_1''^2})^{1/2} R_{u_1''T''}\right)^{1/2}, \tag{4.13}$$

where the last term was written in terms of $R_{u_1''T''}$. Now if we say that (4.9*a*),

$$(\overline{T''^2})^{1/2} = \frac{\tilde{u}_1}{C_p}(\overline{u_1''^2})^{1/2}, \tag{4.14}$$

is empirically valid then (4.13) becomes

$$R_{u_1''T''} = \frac{\overline{T_t''^2}}{2\overline{T''^2}} - 1. \tag{4.15}$$

As expected in the case of negligible total temperature fluctuations this equation reduces to $R_{u_1''T''} = -1$. The value of $R_{u_1''T''}$ predicted by (4.15) agrees well with the actual values (figure 16).

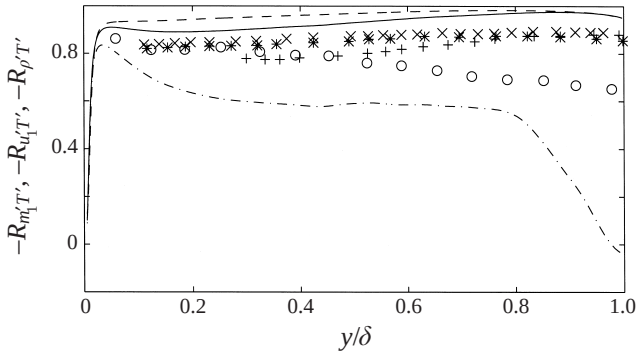

FIGURE 17. Comparison of $-R_{m_1'T'}$, $-R_{u_1'T'}$, and $-R_{\rho'T'}$ versus y/δ: ———, $-R_{m_1'T'}$; – – – –, $-R_{\rho'T'}$; —·—, $-R_{u_1'T'}$; symbols showing the experimental results for $-R_{u_1'T'}$ are the same as in figure 13*a*.

Since for incompressible flow $-R_{u_1'T'}$ is significantly less than unity, the correlation coefficient between streamwise momentum fluctuations and temperature fluctuations, $-R_{m_1'T'}$, will also be much less than unity for incompressible flow (the two are in fact equal). For the compressible simulation, however, $-R_{m_1'T'}$ is much closer to 1 (figure 17). This is because $-R_{m_1'T'}$ is a weighted average of $R_{u_1'T'}$ and $R_{\rho'T'}$, and $R_{\rho'T'}$ is very close to 1 (dashed curve in figure 17) since pressure fluctuations may be assumed to be small compared to density and temperature fluctuations in the equation of state (Lele 1994). The contribution of $R_{\rho'T'}$ to the weighted average pushes $-R_{m_1'T'}$ towards unity. The close correlation between streamwise momentum and temperature fluctuations may indicate a greater similarity between the transport equations for turbulent momentum and heat transport than in the incompressible case, which may be due to a reduction in the importance of the pressure gradient term.

4.2. *'Modified Reynolds analogies'*

Both Gaviglio (1987) and Huang *et al.* (1995) point out that for flows with non-adiabatic boundaries the agreement between (4.9*a*) and measurements is poor. Both authors propose new relationships between temperature and velocity fluctuations which have been called 'modified' Reynolds analogies. Since the agreement of this relation with the current adiabatic wall simulations is not perfect either, we now assess these modified Reynolds analogies. The modified Reynolds analogies of Rubesin (1990), Gaviglio (1987) (GSRA), and Huang *et al.* (1995) (HSRA) all have the form

$$\frac{(\overline{T''^2})^{1/2}/\tilde{T}}{(\gamma-1)\bar{M}^2(\overline{u_1''^2})^{1/2}/\tilde{u}_1} \approx \frac{1}{c(1-a(\partial\tilde{T}_t/\partial\tilde{T}))}. \tag{4.16}$$

If $a = 0$ and $c = 1$ then the standard SRA is obtained. For all the modified expressions $a = 1$. Rubesin used $c = 1.34$. Gaviglio and Huang *et al.* use the mixing length hypothesis to obtain $c = 1.0$ and $c = Pr_t$, respectively. The difference between the derivation of Gaviglio and Huang *et al.* is that Gaviglio assumes that the mixing lengths for temperature and velocity fluctuations are equal. In figure 18 the ratio of the left-hand side of (4.16) to the right-hand side is plotted for the SRA, GSRA, and HSRA. The version presented by Huang *et al.* (1995) is in excellent agreement with the data throughout the boundary layer. The value of $R_{u_1''T''}$ that is predicted by the modified analogy of Huang *et al.* can be derived by substituting equation (4.16), with

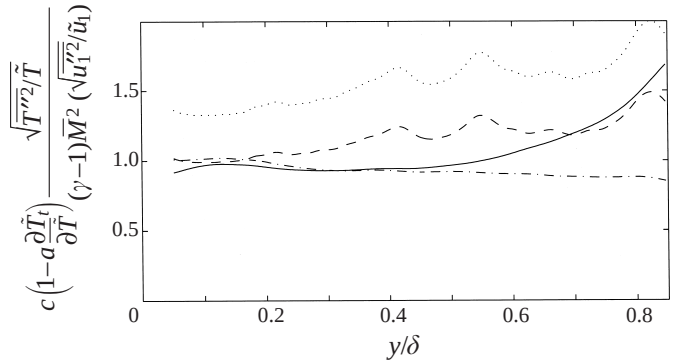

FIGURE 18. Plot of the Strong Reynolds analogy, and the modified Reynolds analogies of Gaviglio (1987) and Huang *et al.* (1995): ———, SRA; – – – –, GSRA; —·—, HSRA; ·····, Rubesin.

$c = Pr_t$, into (4.13) to obtain

$$\frac{[\overline{T_t''^2}/\overline{T''^2} - 1]}{[2Pr_t(1 - \partial\tilde{T}_t/\partial\tilde{T})]} - \frac{Pr_t}{2}\left(1 - \frac{\partial\tilde{T}_t}{\partial\tilde{T}}\right) = 1 + R_{u_1''T''}. \tag{4.17}$$

The profile for $R_{u_1''T''}$ predicted by (4.17) agrees well with the simulation data (figure 16).

Why does the expression of Huang *et al.* work so well? Substituting the definition of the turbulent Prandtl number, (4.9*c*), and the derivative of the total temperature,

$$\frac{\partial\tilde{T}_t}{\partial y} = \frac{\partial\tilde{T}}{\partial y} + \frac{\tilde{u}_1}{C_p}\frac{\partial\tilde{u}_1}{\partial y}, \tag{4.18}$$

into (4.16), with $c = Pr_t$, we obtain

$$\frac{\overline{\rho u_2'' T''}}{(\overline{T''^2})^{1/2}} = -\frac{\overline{\rho u_2'' u_1''}}{(\overline{u_1''^2})^{1/2}}. \tag{4.19}$$

This relationship expresses an analogy between the rates of turbulent heat and momentum transfer normalized by the property that is transported. We may divide through by the RMS of the wall-normal velocity fluctuations to obtain a relationship between the correlation coefficients $R_{u_2''T''}$ and $R_{u_1''u_2''}$:

$$R_{u_2''T''} = -R_{u_1''u_2''}, \tag{4.20}$$

where it is assumed that the correlations $\overline{\rho' u_2'' u_1''}$ and $\overline{\rho' u_2'' T''}$ are small compared to $\bar{\rho}\overline{u_2'' u_1''}$ and $\bar{\rho}\overline{u_2'' T''}$. The simulation results indicate that the two correlation coefficients are very nearly equal throughout the boundary layer (figure 19).

4.3. *Turbulent Prandtl number*

Morkovin was aware that total temperature fluctuations are not negligible compared to temperature fluctuations and stated that another set of expressions could be developed by assuming that $\overline{\rho u_2'' T_t''}$ is much smaller than $\overline{\rho u_2'' T''}$. In the lower half of the boundary layer ($y/\delta < 0.5$) this is a good assumption (figure 20).

Using this assumption, an expression can be developed for the turbulent Prandtl number. Multiplying (4.5) by $\rho u_2''$ and averaging gives

$$\overline{\rho u_2'' T_t''} = \overline{\rho u_2'' T''} + \frac{\tilde{u}_1}{C_p}\overline{\rho u_2'' u_1''}. \tag{4.21}$$

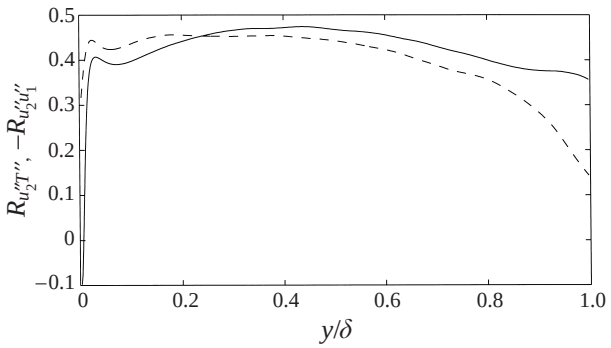

FIGURE 19. Comparison of $R_{u_2''T''}$ and $-R_{u_2''u_1''}$ versus y/δ: ——, $R_{u_2''T''}$; - - - -, $-R_{u_2''u_1''}$.

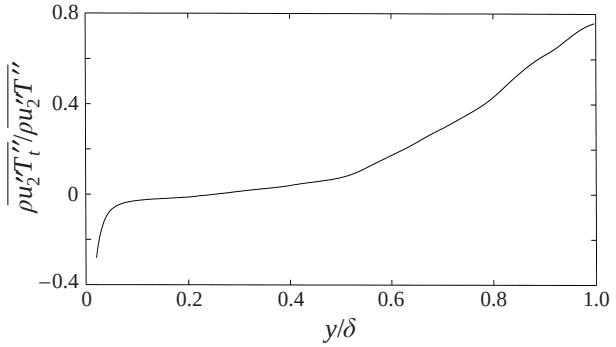

FIGURE 20. Plot of the ratio $\overline{\rho u_2'' T_t''}/\overline{\rho u_2'' T''}$ versus y/δ.

Neglecting $\overline{\rho u_2'' T_t''}$ relative to $\overline{\rho u_2'' T''}$ yields

$$\frac{\overline{\rho u_2'' u_1''}}{\overline{\rho u_2'' T''}} = -\frac{C_p}{\tilde{u}_1}. \tag{4.22}$$

Substituting (4.18) into (4.22) gives

$$Pr_t = \frac{\overline{\rho u_2'' u_1''}}{\overline{\rho u_2'' T''}} \frac{(\partial \tilde{T}/\partial y)}{(\partial \tilde{u}_1/\partial y)} = \frac{\partial \tilde{T}}{\partial y}\left(\frac{\partial \tilde{T}}{\partial y} - \frac{\partial \tilde{T}_t}{\partial y}\right)^{-1}. \tag{4.23}$$

This prediction agrees with the simulation data in the inner portion of the boundary layer, but as the boundary layer edge is approached the agreement becomes poor (figure 21).

5. Turbulent kinetic energy budget

For the benefit of those formulating turbulence models, the budgets for both the Reynolds stresses and the turbulent kinetic energy have been calculated. In this section, the turbulent kinetic energy budget is presented and compared with the incompressible simulations of Spalart (1988). The Reynolds stress budgets are presented in Guarini (1998). Favre averages are used in the analysis to simplify the resulting equations.

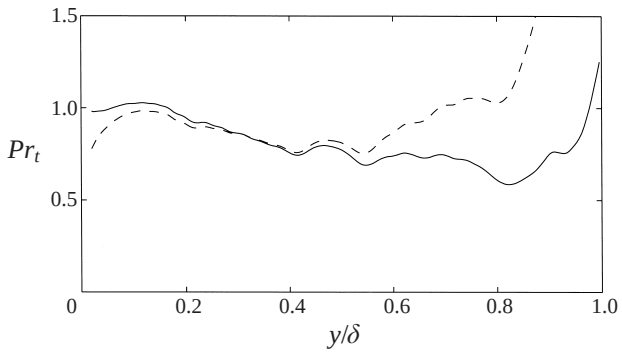

FIGURE 21. Turbulent Prandtl number Pr_t vs. y/δ: ———, time average DNS data; – – – –, Pr_t from (4.23).

The turbulent kinetic energy is defined as:

$$\bar{k} = \frac{1}{2}\frac{\overline{\rho u_i'' u_i''}}{\bar{\rho}}, \tag{5.1}$$

and the turbulent kinetic energy equation is, after assuming homogeneity in the x- and z-directions, given by

$$\frac{\partial}{\partial t}(\bar{\rho}\bar{k}) + \tilde{u}_2\frac{\partial}{\partial x_2}(\bar{\rho}\bar{k}) = P + T + \Pi + D - \phi + V_c. \tag{5.2}$$

The symbols are defined as

$$P = -\overline{\rho u_i'' u_2''}\frac{\partial \tilde{u}_i}{\partial x_2}, \tag{5.3a}$$

$$T = -\frac{1}{2}\frac{\partial}{\partial x_2}\overline{\rho u_i'' u_i'' u_2''}, \tag{5.3b}$$

$$\Pi = \Pi_t + \Pi_d = -\frac{\partial}{\partial x_2}(\overline{u_2'' p'}) + \overline{p'\frac{\partial u_i''}{\partial x_i}}, \tag{5.3c}$$

$$D = \frac{\partial}{\partial x_2}\overline{\frac{u_i''}{Re}\tau_{i2}'}, \tag{5.3d}$$

$$\phi = \overline{\frac{\tau_{il}'}{Re}\frac{\partial u_i''}{\partial x_l}}, \tag{5.3e}$$

$$V_c = -\overline{u_2''}\frac{\partial \bar{p}}{\partial x_2} + \overline{u_i''}\frac{\partial \overline{\tau_{il}}}{\partial x_l} - \bar{\rho}\bar{k}\frac{\partial \tilde{u}_2}{\partial x_2}. \tag{5.3f}$$

The terms in (5.2) can be interpreted as follows: the left-hand side is the substantial derivative of the turbulent kinetic energy along a mean streamline; P is the rate of generation of turbulent kinetic energy by mean velocity gradients; T is turbulent transport; Π are the pressure terms (pressure diffusion and pressure dilatation, respectively); D is viscous diffusion; $-\phi$ is viscous dissipation per unit volume; and finally, V_c includes the terms that arise when the density is not constant. The first two terms of V_c are due to the difference between the Favre and Reynolds average and the last term is the production term due to dilatation. The pressure dilatation as well as the dilatational dissipation, which are not included in V_c, are also due

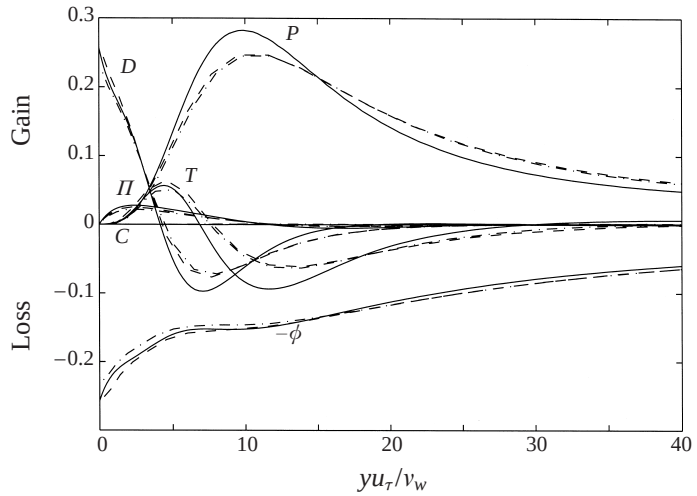

FIGURE 22. Turbulent kinetic energy budget: ———, simulation data; – – – –, Spalart's data $Re_\theta = 1410$; —·—, Spalart's data $Re_\theta = 670$. Symbols are: C, Convective term; P, Generation term; T, Turbulent transport; Π, Pressure terms; D, Viscous transport; $-\phi$, Viscous dissipation.

to non-constant density. In the literature the dissipation per unit mass is commonly referred to as ϵ. Here we use the dissipation per unit volume, which we denote as ϕ for clarity. The dissipation and pressure terms are in a form similar to that given in Huang *et al.* (1995). The compressible turbulent kinetic energy budget agrees with the incompressible results of Spalart at two different Reynolds numbers (figure 22). The generation term is larger than in the incompressible simulation, and the viscous transport and turbulent transport terms are also greater in magnitude than in the incompressible simulation. V_c is small and has not been included on the plot for clarity. Its maximum value is a factor of 25 smaller than that of the generation term.

The effects of compressibility on the dissipation have been of interest in the literature, especially in the context of compressible turbulence models (Zeman 1990 and Sarkar *et al.* 1991). To study dissipation in the current simulation, consider ϕ which can be expanded as

$$\phi = \frac{\bar{\mu}}{Re}\overline{\frac{\partial u_i'}{\partial x_l}\left(\frac{\partial u_i'}{\partial x_l}+\frac{\partial u_l'}{\partial x_i}-\frac{2}{3}\delta_{il}\frac{\partial u_k'}{\partial x_k}\right)}+\overline{\frac{\mu'}{Re}\frac{\partial u_i'}{\partial x_l}\left(\frac{\partial u_i'}{\partial x_l}+\frac{\partial u_l'}{\partial x_i}-\frac{2}{3}\delta_{il}\frac{\partial u_k'}{\partial x_k}\right)}$$
$$+\overline{\frac{\mu'}{Re}\frac{\partial u_i'}{\partial x_l}\left(\frac{\partial \bar{u}_i}{\partial x_l}+\frac{\partial \bar{u}_l}{\partial x_i}-\frac{2}{3}\delta_{il}\frac{\partial \bar{u}_k}{\partial x_k}\right)}, \qquad (5.4)$$

where the three terms in this expression will be referred to as ϕ_1, ϕ_2, and ϕ_3, respectively. The fluctuations about the Favre average in (5.3*e*) have been replaced using the identity

$$\overline{\frac{\tau_{il}'}{Re}\frac{\partial u_i''}{\partial x_l}}=\overline{\frac{\tau_{il}'}{Re}\frac{\partial u_i'}{\partial x_l}}. \qquad (5.5)$$

The terms, ϕ_2 and ϕ_3, which involve viscosity fluctuations, are negligible compared to ϕ_1 in this simulation.

The first term, ϕ_1, can be decomposed into parts that are more amenable to

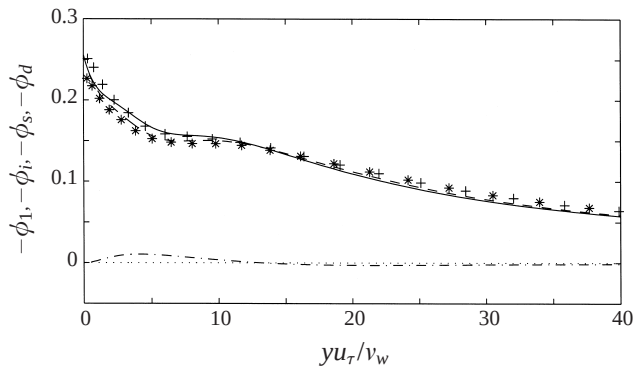

FIGURE 23. Comparison of dissipation terms: ———, $-\phi_1 = -(\phi_s + \phi_i + \phi_d)$; – – – –, solenoidal dissipation $(-\phi_s)$; —·—, dissipation due to inhomogeneity $(-\phi_i)$; ·····, dissipation due to dilatation $-\phi_d$; +, Spalart's data $Re_\theta = 1410$; *, Spalart's data $Re_\theta = 670$.

comparison with incompressible flows by expressing velocity gradients in terms of the rate-of-deformation tensor, S'_{li}, and spin tensor, Ω'_{li}, which is related to the vorticity through $\Omega'_{ij}\Omega'_{ij} = \omega'_i\omega'_i/2$. Simplifying gives for ϕ_1:

$$\phi_1 = \frac{\bar{\mu}}{Re}\overline{\omega'_i\omega'_i} + 2\frac{\bar{\mu}}{Re}\left(\frac{\partial^2}{\partial x_i \partial x_l}\overline{u'_i u'_l} - 2\frac{\partial}{\partial x_l}\overline{u'_l\frac{\partial u'_i}{\partial x_i}}\right) + \frac{4}{3}\frac{\bar{\mu}}{Re}\overline{\frac{\partial u'_i}{\partial x_i}\frac{\partial u'_k}{\partial x_k}}, \tag{5.6}$$

where the first term on the right is the homogeneous incompressible dissipation, or the solenoidal part of the dissipation, ϕ_s, the second term, ϕ_i, is due to inhomogeneity, and the third term, ϕ_d, is due to dilatation. Both the dissipation due to dilatation and inhomogeneity are very small compared to the solenoidal dissipation (figure 23). At the wall the dissipation due to inhomogeneity provides a very slight contribution to the total dissipation. The compressible result agrees well with the incompressible results of Spalart.

Finally, we consider the pressure terms. There are three: pressure diffusion (Π_t), pressure dilatation (Π_d), and compressibility (Π_c). The pressure dilatation term is also associated with compressibility effects, since the dilatation is zero for an incompressible flow. The three pressure terms are

$$\Pi_t = -\frac{\partial\overline{u''_2 p'}}{\partial x_2}, \quad \Pi_d = \overline{p'\frac{\partial u''_i}{\partial x_i}}, \quad \Pi_c = -\overline{u''_2}\frac{\partial \bar{p}}{\partial x_2}. \tag{5.7a–c}$$

Of the three, Π_d and Π_c are much smaller than Π_t near the wall (figure 24). In fact, the sum of the pressure terms is almost indistinguishable from Π_t in the wall region, which shows that the compressibility terms have very little effect on the overall contribution of the pressure terms to the turbulent kinetic energy budget. Away from the wall, all the terms are small and the compressibility term contributes to the sum of the terms. The pressure diffusion term is larger than the value obtained by Spalart in both his $Re_\theta = 1410$ and $Re_\theta = 670$ cases.

The results and analysis given here show that at $M = 2.5$, the effects of compressibility on the turbulent kinetic energy balance are not due to the new compressibility terms that appear in the equations. Instead, the effects are more subtle, quantitatively affecting the terms that appear in the incompressible case.

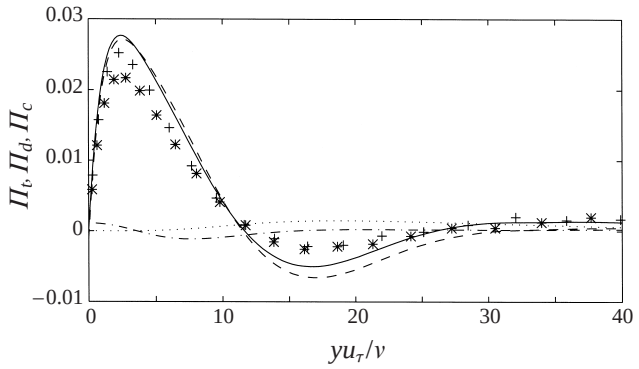

FIGURE 24. Comparison of pressure terms: ———, $\Pi_t + \Pi_d + \Pi_c$; – – – –, Π_t; —·—, Π_d; ·····, Π_c; +, Spalart's data $Re_\theta = 1410$; *, Spalart's data $Re_\theta = 670$.

6. Conclusions

A direct numerical simulation of a Mach 2.5 turbulent boundary layer was carried out using the method described in the Appendix. The Reynolds number of the simulation was $Re_{\theta'} = 849$. Comparison with available experiments and with other simulations (i.e. those of Spalart) suggest that the current simulation provides an accurate description of a compressible turbulent boundary layer.

It was shown that many of the scaling relations used to express compressible boundary layer statistics in terms of those for incompressible boundary layers are consistent with the current simulation. In particular, we have shown that the Van Driest transformed velocity behaves much the same as the streamwise velocity in the incompressible case. There was a small logarithmic region with $\kappa = 0.40$ and $C = 4.7$. It was also shown that the RMS velocity fluctuations are collapsed with incompressible results by the mean density scaling suggested by Morkovin. When this scaling is applied, the data from the current simulation agree remarkably well with Spalart's $Re_\theta = 670$ and $Re_\theta = 1410$ simulations. The mean density scaling of $\overline{u'v'}$ also results in a fairly good collapse with incompressible results.

An inconsistency with the standard analysis of compressible turbulent boundary layers was found in that the total temperature fluctuations were of the same order as temperature fluctuations. This invalidates many of the assumptions made in deriving the strong Reynolds analogy (SRA). However, the relationship between RMS temperature and streamwise velocity fluctuations, (4.9*a*), agreed with the simulation data reasonably well nonetheless. A condition for the validity of the RMS relationship in the presence of significant total temperature fluctuations was derived, (4.12), and this condition is satisfied by the simulation data. An expression for the correlation coefficient $R_{u_1''T''}$ derived by Gaviglio (4.15) using the RMS relationship agrees very well with the simulation data.

The low value of the correlation coefficient found in the simulations indicates that instantaneous relationships between temperature and velocity fluctuations, (4.8) for example, are invalid. Experimental evidence, however, suggests a much higher value of the correlation coefficient than was found in this simulation. It appears that this difference between experiments and the current simulation can be due to a difference of about a factor of 2 in the magnitude of the total temperature fluctuations, with the experimental values being smaller. The reason for this is not known.

The modified Reynolds analogy of Huang *et al.* showed better agreement with

the simulation data than Gaviglio's modified Reynolds analogy and the original expression of Morkovin. Using Huang *et al.*'s modified analogy, a relationship between the rate of turbulent heat transfer and turbulent momentum transfer was derived and shown to agree with the simulation data. The streamwise momentum and temperature fluctuations were found to be very highly correlated throughout the boundary layer with a correlation coefficient $0.88 \leqslant -R_{m_1' T'} \leqslant 1$. This is in contrast to the low correlation between the velocity and thermal fields away from the wall and also stands in contrast to the lack of correlation between streamwise momentum and temperature in the incompressible case (where velocity and momentum are proportional).

The turbulent kinetic energy budget was calculated and compared with those of Spalart's incompressible simulations. The peak rate of production was found to be larger than for the incompressible case. This is balanced by an increase in the magnitude of turbulent transport and viscous transport when compared to the incompressible simulations. Some of this difference might be attributable to the different small-scale resolution used in these two simulations, with the current simulation having better resolution than the simulations of Spalart. Balances for the terms in the Reynolds stress tensor have been computed and are presented in Guarini (1998).

The authors would like to thank NASA's Numerical Aerodynamic Simulation facility (NAS) and the Air Force Aeronautical Systems Center (ASC) Major Shared Resource Center (MSRC) for their computational support. The simulation and code development were done on the Cray C-90 supercomputers at these two facilities. The support of a NASA Graduate Student Researchers Program grant (NGT 2-52209) and AFOSR grant F49620-97-1-0089 is gratefully acknowledged by the first and second authors, respectively.

Appendix. Theoretical development

In this appendix we review Spalart's transformation and apply it to the compressible boundary layer. This involves the development of a generalized coordinate system in which boundary layer growth is minimal, the definition of the two scales involved in the problem, the transformation of the Navier–Stokes equations to the new curvilinear coordinate system, and the calculation of the slow-growth terms. This analysis for the compressible case mirrors that developed by Spalart (Spalart & Leonard 1987; Spalart 1988) for the incompressible boundary layer. The particulars of that analysis that are directly relevant to the current development are recalled briefly in § A.2 and § A.3 to fix the ideas and the nomenclature.

A.1. *Equations*

The form of the Navier–Stokes equations is chosen for computational convenience. The energy equation is transformed so that pressure is a state variable instead of energy. The fluid variables, u_i, $m_i = \rho u_i$, p, and $\sigma = (1/\rho)$ are non-dimensionalized by a_o, $\rho_o a_o$, $\rho_o a_o^2$, and $(1/\rho_o)$, respectively. Lengths are non-dimensionalized by δ_o and times by (δ_o/a_o). Then the Navier–Stokes equations become

$$\frac{\partial \sigma}{\partial t} = \sigma^2 \frac{\partial m_j}{\partial x_j}, \tag{A 1a}$$

$$\frac{\partial m_i}{\partial t} = -\frac{\partial}{\partial x_j}(\sigma m_i m_j) - \frac{\partial p}{\partial x_i} + \frac{1}{Re}\frac{\partial \tau_{ij}}{\partial x_j}, \tag{A 1b}$$

$$\frac{\partial p}{\partial t} = -\frac{\partial p u_j}{\partial x_j} - (\gamma - 1) p \frac{\partial u_j}{\partial x_j} + \left(\frac{\gamma - 1}{Re}\right) \tau_{ij} \frac{\partial u_i}{\partial x_j} + \frac{1}{RePr}\frac{\partial q_j}{\partial x_j}. \tag{A 1c}$$

The Reynolds number is $Re = (\rho_o a_o \delta_o)/\mu_o$ and the Prandtl number is $Pr = (\mu C_p)/k$. The Fourier heat conduction law, q_j, is given by

$$q_j = \mu \frac{\partial T}{\partial x_j}, \tag{A 2}$$

and the stress, τ_{ij}, is

$$\tau_{ij} = \mu \left(\frac{\partial u_i}{\partial x_j} + \frac{\partial u_j}{\partial x_i} - \frac{2}{3}\delta_{ij} \frac{\partial u_k}{\partial x_k} \right). \tag{A 3}$$

The temperature, T, is non-dimensionalized by $T_o \equiv a_o^2/(\gamma R)$, such that the equation of state, $T = \gamma \sigma P$, results.

A.2. *Coordinate system*

Following Spalart (Spalart & Leonard 1987; Spalart 1988), the Navier–Stokes equations are transformed into a coordinate system that is fitted to the growing boundary layer. The new coordinate system is (ξ,η,z), where

$$\xi = x \quad \text{and} \quad \eta = \eta(x, y). \tag{A 4}$$

Curves of $\eta = \text{const.}$ are slightly inclined to the wall with a slope $\tilde{S}(\xi, \eta)$ chosen in such a way that we fit the growth of both the boundary layer and the viscous sublayer. This coordinate system is selected so that when a small section of the boundary layer is simulated, the variation of the mean fluid dynamic variables along a constant-η curve is so small that approximate homogeneity will hold.

The Jacobian of the transformation involves two parameters, $\tilde{S}$ and $\tilde{T}$, where

$$\tilde{S} \equiv \left.\frac{\partial y}{\partial \xi}\right|_{\eta,z} \quad \text{and} \quad \tilde{T} \equiv \left.\frac{\partial y}{\partial \eta}\right|_{\xi,z}. \tag{A 5}$$

The quantity $\tilde{S}$ gives the slope of the constant-η curves, while $\tilde{T}$ is the local stretching between the y- and η-coordinates, and $\tilde{S}_\eta = \tilde{T}_\xi$ follows from (A 5). In terms of $\tilde{S}$ and $\tilde{T}$, the Jacobian is given by

$$\begin{Bmatrix} \partial/\partial x \\ \partial/\partial y \\ \partial/\partial z \end{Bmatrix} = \begin{bmatrix} 1 & -\tilde{S}/\tilde{T} & 0 \\ 0 & 1/\tilde{T} & 0 \\ 0 & 0 & 1 \end{bmatrix} \begin{Bmatrix} \partial/\partial \xi \\ \partial/\partial \eta \\ \partial/\partial z \end{Bmatrix}. \tag{A 6}$$

A.3. *Multiple-scale analysis*

Even in the transformed coordinate system, the mean variables evolve slowly in ξ. The fluctuations also have a slow variation in intensity at constant η. Thus, for example, we approximate

$$u'(\xi, \eta, z, t) = A_u(\xi, \eta) u_p(\xi, \eta, z, t), \tag{A 7}$$

where A_u is a slowly varying amplitude and u_p is homogeneous, so that in the simulation it can be treated as periodic in ξ. The subscript on A refers to the fluid dynamic variable with which it is associated. The fluctuations of the other state variables may be similarly decomposed. After introducing a slow variable $\Xi = \epsilon\xi$ and a fast variable ξ, and using the techniques of multiple-scale asymptotics, decomposition of the velocity into a mean and fluctuating part yields

$$u(\xi, \Xi, \eta, z, t) = U(\Xi, \eta) + A_u(\Xi, \eta) u_p(\xi, \eta, z, t), \tag{A 8}$$

and the derivative in the streamwise direction becomes

$$\frac{\partial u}{\partial \xi} = \epsilon \frac{\partial U}{\partial \Xi} + A_u \frac{\partial u_p}{\partial \xi} + \epsilon u_p \frac{\partial A_u}{\partial \Xi}. \tag{A 9}$$

Using (A 7) this can be rewritten in the compact form

$$u_\xi = \epsilon U_\Xi + u'_\xi + \epsilon u'_\Xi, \tag{A 10}$$

where $u'_\Xi = A_{u_\Xi} u'/A_u$.

To allow $u'_\Xi = A_{u_\Xi} u'/A_u$ to be determined in the actual simulation, note that

$$\frac{A_{u\Xi}}{A_u} = \frac{(u'_{rms})_\Xi}{u'_{rms}}. \tag{A 11}$$

The coordinate system is also slowly varying in ξ and hence $y = y(\Xi, \eta)$, so that (A 5) is rewritten as

$$\tilde{S} = \epsilon \frac{\partial y}{\partial \Xi}\bigg|_{\eta,z} \qquad \text{and} \qquad \tilde{T} = \frac{\partial y}{\partial \eta}\bigg|_{\Xi,z}. \tag{A 12}$$

The simulations can be regarded as being performed at a fixed value $\Xi = \Xi_0$ of the slow variable. We are then free to choose η such that $y(\Xi_0, \eta) = \eta$ which implies $\tilde{T}(\Xi_0, \eta) = 1$. We define S such that $\tilde{S} = \epsilon S$.

A.4. *Modified Navier–Stokes equations*

Using the definitions above and replacing derivatives in ξ with slow and fast derivatives gives the transformed Navier–Stokes equations, that contain several additional terms, shown enclosed in square brackets:

$$\frac{\partial \sigma}{\partial t} = \sigma^2 \frac{\partial m_j}{\partial \xi_j} + \epsilon \left[-S\sigma^2 \frac{\partial m_1}{\partial \eta} \right] + \epsilon[-(\bar{\sigma}_\Xi + \sigma'_\Xi)\sigma m_1 + \sigma(U_\Xi + u'_\Xi)], \tag{A 13a}$$

$$\frac{\partial m_1}{\partial t} = -\frac{\partial}{\partial \xi_j}(\sigma m_1 m_j) - \frac{\partial p}{\partial \xi} + \frac{1}{Re}\frac{\partial \tau_{1j}}{\partial \xi_j} + \epsilon \left[S\frac{\partial}{\partial \eta}(u_1 m_1) + S\frac{\partial p}{\partial \eta} \right]$$
$$+\epsilon[(\bar{\sigma}_\Xi + \sigma'_\Xi)m_1^2 - 2(U_\Xi + u'_\Xi)m_1 - (\bar{p}_\Xi + p'_\Xi)], \tag{A 13b}$$

$$\frac{\partial m_2}{\partial t} = -\frac{\partial}{\partial \xi_j}(\sigma m_2 m_j) - \frac{\partial p}{\partial \eta} + \frac{1}{Re}\frac{\partial \tau_{2j}}{\partial \xi_j} + \epsilon \left[\frac{S}{2}\frac{\partial}{\partial \eta}(u_1 m_2 + u_2 m_1) \right]$$
$$+\epsilon[(\bar{\sigma}_\Xi + \sigma'_\Xi)m_1 m_2 - (U_\Xi + u'_\Xi)m_2 - (V_\Xi + v'_\Xi)m_1], \tag{A 13c}$$

$$\frac{\partial m_3}{\partial t} = -\frac{\partial}{\partial \xi_j}(\sigma m_3 m_j) - \frac{\partial p}{\partial z} + \frac{1}{Re}\frac{\partial \tau_{3j}}{\partial \xi_j} + \epsilon \left[\frac{S}{2}\frac{\partial}{\partial \eta}(u_3 m_1 + u_1 m_3) \right]$$
$$+\epsilon[(\bar{\sigma}_\Xi + \sigma'_\Xi)m_1 m_3 - (W_\Xi + w'_\Xi)m_1 - (U_\Xi + u'_\Xi)m_3], \tag{A 13d}$$

$$\frac{\partial p}{\partial t} = -\frac{\partial p u_j}{\partial \xi_j} - (\gamma - 1)p\frac{\partial u_j}{\partial \xi_j} + (\frac{\gamma - 1}{Re})\tau_{ij}\frac{\partial u_i}{\partial \xi_j} + \frac{1}{RePr}\frac{\partial q_j}{\partial \xi_j}$$
$$+\epsilon \left[S\frac{\partial}{\partial \eta}(p u_1) + S(\gamma - 1)p\frac{\partial u_1}{\partial \eta} \right] + \epsilon[-(\bar{p}_\Xi + p'_\Xi)\sigma m_1 - (U_\Xi + u'_\Xi)\gamma p]. \tag{A 13e}$$

Note that all additional viscous terms have been neglected, since they are all multiplied by (S/Re), which is small. In particular, near the wall, where the viscous terms are large, the value of S is approximately zero. The terms in square brackets are the corrections to the original Navier–Stokes equations that account for boundary layer growth. In each equation the first set of bracketed terms results from the coordinate transformation and the second set results from the multiple-scale analysis. These equations will be solved in a finite domain in the fast variable ξ. Thus, in the solution domain, functions of the slow variable Ξ can be taken as constant (functions of y) and the fluctuating quantities can be taken as homogeneous in the fast variable.

A.5. *Slow derivatives of mean quantities*

Before the modified equations (A 13) can be solved numerically, the slow derivatives must be determined in terms of the simulation solution variables. For any arbitrary slowly varying function f, $f_\Xi = f_\xi/\epsilon$. In what follows, it will be convenient to determine relations for f_ξ rather than f_Ξ. The slow derivatives of the mean thermodynamic quantities are calculated using the Van Driest (1955) temperature–velocity relationship as given by Walz (Fernholz & Finley 1980),

$$\frac{\bar{T}}{\bar{T}_\infty} = 1 + r\frac{\gamma-1}{2}M_\infty^2\left[1-\left(\frac{\bar{u}}{\bar{u}_\infty}\right)^2\right], \tag{A 14}$$

where the recovery factor, r, is taken to be $r = 0.896$. Equation (A 14) was found to be valid *a posteriori* in the simulations. Differentiating (A 14), the temperature derivative is expressed in terms of the mean velocity:

$$\frac{\bar{T}_\xi}{\bar{T}_\infty} = -r(\gamma-1)M_\infty^2\left(\frac{\bar{u}}{\bar{u}_\infty}\right)\left(\frac{\bar{u}_\xi}{\bar{u}_\infty}\right). \tag{A 15}$$

Since the pressure gradient, $\bar{p}_\xi$, is zero we get

$$\frac{\bar{\rho}_\xi}{\bar{\rho}} = -\frac{\bar{T}_\xi}{\bar{T}}. \tag{A 16}$$

Introducing means and fluctuations into the relationship $\sigma\rho = 1$, averaging, and neglecting $\overline{\sigma'\rho'}$ gives after differentiation

$$\frac{\bar{\sigma}_\xi}{\bar{\sigma}} = -\frac{\bar{\rho}_\xi}{\bar{\rho}}. \tag{A 17}$$

Thus all the slow derivatives of mean thermodynamic variables are related directly to the slow derivative of the mean streamwise velocity.

For his incompressible simulation at the first station, Spalart used the well-known scaling laws for the mean streamwise velocity to calculate its slow derivatives. There is no equivalent scaling for compressible flow. However, the Van Driest transformation allows one to define a transformed velocity which satisfies the incompressible scalings. This transformation was found to be valid *a posteriori* in the simulations (see § 3.1). In the definition of the van Driest transformed velocity, U_c (3.2), $\sqrt{\bar{T}_w/\bar{T}}$ is a function of ξ and U. Differentiating (3.2) with respect to ξ yields

$$\frac{\partial U_c(\xi,\eta)}{\partial\xi} = \int_0^{U(\xi,\eta)}\frac{\partial}{\partial\xi}\left(\frac{\bar{T}_w}{\bar{T}}\right)^{1/2}\mathrm{d}U + \left(\frac{\bar{T}_w}{\bar{T}}\right)^{1/2}\Bigg|_{U(\xi,\eta)}\frac{\partial U(\xi,\eta)}{\partial\xi}. \tag{A 18}$$

Now, the Van Driest temperature–velocity relationship (A 14) implies that temperature is a function of U alone provided the recovery factor, r, is independent of ξ.

Experiments have verified that this assumption is valid (Fernholz & Finley 1980). The first term in (A 18) is therefore zero yielding

$$U_\xi = \left(\frac{\bar{T}}{\bar{T}_w}\right)^{1/2} U_{c_\xi}. \tag{A 19}$$

To obtain U_{c_ξ} (or U_ξ) for use in the modified Navier–Stokes equations (A 13), the strategy is to develop a relationship between U_{c_ξ} and U_c using well-known model profiles for the velocity U_c. Then U_{c_ξ} can be calculated from U_c as determined in the simulation. Note that model profiles discussed below are used *only to evaluate slow derivatives*. The mean velocity profile is determined from the simulation *not from the model profiles*.

To develop an expression for U_{c_ξ}, a model profile for U_c that is valid across the entire boundary layer is needed. Since U_c is the Van Driest transformed velocity, we can use a model profile for the incompressible boundary layer, in particular, we use the relation of Coles (1956):

$$\frac{U_{c_m}}{u_\tau} = \begin{cases} U_{c_b}/u_\tau + (\Pi/\kappa)w(y/\delta), & y \leqslant \delta, \\ U_{c_\infty}/u_\tau, & y > \delta, \end{cases} \tag{A 20}$$

where U_{c_b} is a basic law-of-the-wall profile and $w(y/\delta)$ is a wake function. In order to distinguish the model profile from that of the simulation, the model profile is denoted by U_{c_m}. For the basic profile and wake function we use the relations of Reichardt (1951) and Finley (Cebeci & Bradshaw 1977), respectively:

$$\frac{U_{c_b}}{u_\tau} = \frac{1}{\kappa}\ln\left(1+\kappa\frac{yu_\tau}{v_w}\right) + C_1\left[1 - \mathrm{e}^{-yu_\tau/(\eta_1 v_w)} - \left(\frac{yu_\tau}{\eta_1 v_w}\right)\mathrm{e}^{-yu_\tau b/v_w}\right], \tag{A 21}$$

and

$$\Pi w\left(\frac{y}{\delta}\right) = \left(\frac{y}{\delta}\right)^2 - \left(\frac{y}{\delta}\right)^3 + 6\Pi\left(\frac{y}{\delta}\right)^2 - 4\Pi\left(\frac{y}{\delta}\right)^3. \tag{A 22}$$

Several of the constants in these expressions are prescribed, that is $C_1 = -(1/\kappa)\ln(\kappa) + C$, $\eta_1 = 11$, and $b = 0.33$. The constants, u_τ, κ, and C are calculated from the simulation mean velocity profile at each time step. This leaves two parameters, δ and Π, which are determined by matching the properties of the model profile to the instantaneous simulation mean velocity profile. This profile is a good representation of the mean velocity throughout the boundary layer (see figure 5). Reichardt's profile is used instead of the classic profile of Coles because it captures both the linear sub-layer behaviour, where $U_c^+ = y^+$, and also the logarithmic behaviour of the mean velocity profile. The standard log-law becomes infinite at the wall which is undesirable in a simulation.

The parameters, δ and Π are set so that the free-stream velocity U_{c_∞} and the transformed displacement thickness of the model profile U_{c_m} match those in the simulation. Thus we have

$$U_{c_\infty} = U_{c_m}(\delta), \tag{A 23a}$$

$$\int_0^\infty \left(1 - \frac{U_c}{U_{c_\infty}}\right)\mathrm{d}y = \int_0^\delta \left(1 - \frac{U_{c_m}}{U_{c_\infty}}\right)\mathrm{d}y. \tag{A 23b}$$

These relations lead to a nonlinear system of equations for δ and Π (see Guarini 1998).

The slow derivative U_{c_ξ} can be written as

$$\frac{U_{c_\xi}}{u_\tau} = \frac{u_{\tau_\xi}}{u_\tau}\left(\frac{U_c}{u_\tau}\right) + \frac{\partial}{\partial \xi}\left(\frac{U_c}{u_\tau}\right). \tag{A 24}$$

Using the model profile to evaluate the derivative, (A 24) can be written

$$\frac{U_{c_\xi}}{u_\tau} = \frac{u_{\tau_\xi}}{u_\tau}\left(\frac{U_c}{u_\tau}\right) + \frac{\partial U_{c_m}}{\partial \delta}\delta_\xi + \frac{\partial U_{c_m}}{\partial u_\tau}u_{\tau_\xi} + \frac{\partial U_{c_m}}{\partial \Pi}\Pi_\xi, \tag{A 25}$$

leaving just u_{τ_ξ}, δ_ξ, and Π_ξ to be determined. It is known that Π becomes independent of Reynolds number for $Re_\theta > 5000$ (Cebeci & Bradshaw 1977) and that the variation of Π for lower Reynolds numbers is very small, thus the approximation $\Pi_\xi = 0$ is used. Since $U_{c_{\infty_\xi}} = 0$, (A 25) can be evaluated at $y = \delta$ to obtain a relation between u_{τ_ξ}/u_τ and δ_ξ/δ:

$$\frac{u_{\tau_\xi}}{u_\tau} = -\frac{(u_\tau^2\delta/U_{c_\infty}\nu_w)\{(1+\kappa\delta u_\tau/\nu_w)^{-1}+R\}}{(u_\tau^2\delta/U_{c_\infty}\nu_w)\{(1+\kappa\delta u_\tau/\nu_w)^{-1}+R\}+1}\left(\frac{\delta_\xi}{\delta}\right), \tag{A 26}$$

where

$$R = \frac{C_1}{\eta_1}\left[\mathrm{e}^{-\delta u_\tau/(\nu_w\eta_1)} + \left(\frac{\delta u_\tau b}{\nu_w} - 1\right)\mathrm{e}^{-\delta u_\tau b/\nu_w}\right], \tag{A 27}$$

and the assumption $S(y=\delta) = \delta_\xi/\delta$ has been made. To find δ_ξ/δ, the momentum integral equation, and the assumption $\delta_\xi/\delta = \theta_\xi/\theta$ (constant shape factor) is used to obtain

$$\frac{\delta_\xi}{\delta} = \frac{\tau_w}{\theta\bar{\rho}_\infty U_\infty^2}. \tag{A 28}$$

This closes the system of equations for U_{c_ξ}/u_τ.

Since the slowly varying amplitude functions are proportional to the RMS fluctuations, we can calculate the slow derivative of the velocity fluctuations by assuming a similar scaling law as was used by Spalart for his simulations, which yields

$$\frac{A_{vi_\xi}}{A_{vi}} = \frac{u_{\tau_\xi}}{u_\tau}. \tag{A 29}$$

Since the simulation results show that the scaling used in the incompressible case is modified by the mean density profile, (A 29) could be improved by including this scaling.

To determine the metric S we take the first derivative with respect to ξ of the following expression given by Spalart (1988):

$$\eta_s = \frac{y_2^p(c_4 y^+) + y^p(y/\delta)}{y_2^p + y^p}, \tag{A 30}$$

where $y_2 = (y_1 y_3)^{1/2}$, $y_1 u_\tau/\nu_w = c_1$, $y_3/\delta = c_2$, and $p = c_3/\log_{10}(y_3/y_1)$. Spalart's choices for the constants c_1, c_2, c_3, and c_4 are 0.5, 0.3, 5.0, and 0.001, respectively; η_s is a weighted average of wall units and y/δ units. It should be noted that the quantity η_s is not the same as η and does not satisfy the conditions $y = \eta$ and $T = 1$ at the station of the simulation. Nonetheless, η_s can be used to calculate $\tilde{S}$ since it follows the growth of the boundary layer and viscous sublayer (see Spalart 1988).

All the slow terms in (A 13) can now be determined from the simulated quantities, thus closing the equations.

REFERENCES

Adams, N. A., Maeder, T., Guo, Y. & Kleiser, L. 1998 Direct simulation of turbulent supersonic boundary layers by an extended temporal approach. Submitted to *J. Fluid Mech.*

Bardina, J. E., Huang, P. G. & Coakley, T. J. 1980 Turbulence modeling validation, testing, and development. *NASA Tech. Mem.* 110446.

Bell, D. M. & Ferziger, J. H. 1993 Turbulent boundary layer DNS with passive scalars. In *Near-Wall Turbulent Flows* (ed. R. M. C. So, C. G. Speziale, B. E. Launder), pp. 327–336. Elsevier.

Bertolotti, F. P., Herbert, Th. & Spalart, P. R. 1992 Linear and nonlinear stability of the Blasius boundary layer. *J. Fluid Mech.* **242**, 441–474.

Cebeci, T. & Bradshaw, P. 1977 *Momentum Transfer in Boundary Layers*. Hemisphere.

Coleman, G. N., Kim, J. & Moser, R. D. 1995 A numerical study of turbulent supersonic isothermal-wall channel flow. *J. Fluid Mech.* **305**, 159–183.

Coles, D. 1954 Measurements of turbulent friction on a smooth flat plate in supersonic flow *J. Aero. Sci.* **21**, 433–448.

Coles, D. 1956 The law of the wake in the turbulent boundary layer. *J. Fluid Mech.* **1**, 191–226.

De Boor, C. 1978 *A Practical Guide to Splines*. Springer.

Eléna, M. & Gaviglio, J. 1993 Compressible turbulent boundary layer: survey of methods of analysis and results. *La Recherche Aérospatiale* **2**, 1–21.

Fernholz, H. H & Finley, P. J. 1980 A critical commentary on mean flow data for two-dimensional compressible boundary layers. *AGARD-AG*-253.

Gaviglio, J. 1987 Reynolds analogies and experimental study of heat transfer in the supersonic boundary layer. *Intl J. Heat Mass Transfer*. **30**, 911–926.

Giles, M. B. 1989 Non-reflecting boundary conditions for Euler equation calculations. *AIAA* 89-1942-CP.

Giles, M. B. 1990 Nonreflecting boundary conditions for Euler equation calculations. *AIAA J.* **28**, 2050–2058.

Guarini, S. 1998 Direct numerical simulation of supersonic turbulent boundary layers. PhD thesis, Stanford University.

Guo, Y. & Adams, N. A. 1994 Numerical investigation of supersonic turbulent boundary layers with high wall temperature. In *Proc. 1994 Summer Program of the Center for Turbulence Research, Stanford University*, pp. 245–267.

Hatay, F. F. & Biringen, S. 1995 Direct numerical simulation of low-Reynolds number supersonic turbulent boundary layers. *AIAA Paper* 95-0581.

Huang, P. G., Coleman, G. N. & Bradshaw, P. 1995 Compressible turbulent channel flows: DNS results and modeling. *J. Fluid Mech.* **305**, 185–218.

Jimenez, J. & Moin, P. 1991 The minimal flow unit in near-wall turbulence. *J. Fluid Mech.* **225**, 213–240.

Kim, J., Moin, P. & Moser, R. 1987 Turbulence statistics in fully developed channel flow at low Reynolds number. *J. Fluid Mech.* **177**, 133–166.

Kistler, A. L. 1959 Fluctuation measurements in a supersonic turbulent boundary layer. *Phys. Fluids* **2**, 290–296.

Kravchenko, A. G., Moin, P. & Moser, R. D. 1996 Zonal embedded grids for numerical simulation of wall-bounded turbulent flows. *J. Comput. Phys.* **127**, 412–423.

Laufer, J. 1964 Some statistical properties of the pressure field radiated by a turbulent boundary layer. *Phys. Fluids* **7**, 1191–1197.

Lele, S. K. 1994 Compressibility effects on turbulence. *Ann. Rev. Fluid Mech.* **26**, 211–254.

Loulou, P. 1996 Direct numerical simulation of incompressible pipe flow using a b-spline spectral method. PhD thesis, Stanford University.

Lund, T. S., Wu, X. & Squires K. D. 1998 Generation of turbulent inflow data for spatially-developing boundary layer simulations. *J. Comput. Phys.* **140**, 233–258.

Morkovin, M. V. 1962 Effects of compressibility on turbulent flows. In *Mécanique de la Turbulence* (ed. A. Favre) CNRS, pp. 367–380.

Rai, M. M., Gatski, T. B. & Erlebacher, G. 1995 Direct simulation of spatially evolving compressible turbulent boundary layers. *AIAA Paper* 95-0583.

Rao, R. 1997 Direct numerical simulation of turbulent supersonic jets. PhD thesis, University of Minnesota.

Reichardt, H. 1951 Complete representation of the turbulent velocity distribution in smooth pipes. *Z. Angew Math. Mech.* **31**, 208–219.

Rubesin, M. W. 1990 Extra compressibility terms for Favre-averaged two-equations models of inhomogeneous turbulent flows. *NASA CR*-177556.

Sarkar, S. 1995 The stabilizing effect of compressibility in turbulent shear flow. *J. Fluid Mech.* **282**, 163–186.

Sarkar, S., Erlebacher, G., Hussaini, M. Y. & Kreiss, H. O. 1991 The analysis and modeling of dilatational terms in compressible turbulence. *J. Fluid Mech.* **227**, 473–493.

Shariff, K. & Moser, R. D. 1998 Two-dimensional mesh embedding for B-spline methods. *J. Comput. Phys.* **145**, 471–488.

Smith, D. R. & Smits, A. J. 1993 Simultaneous measurement of velocity and temperature fluctuations in the boundary layer of a supersonic flow. *Exp. Thermal Fluid Sci.* **7**, 221–229.

Smits, A. J. & Dussauge, J. P. 1996 *Turbulent Shear Layers in Supersonic Flow*. American Institute of Physics.

Spalart, P. R. 1988 Direct simulation of a turbulent boundary layer up to $R_\theta = 1410$. *J. Fluid Mech.* **187**, 61–98.

Spalart, P. R. & Leonard, A. 1987 Direct numerical simulation of equilibrium turbulent boundary layers. In *Turbulent Shear Flows 5* (ed. F. J. Durst *et al.*) Springer, pp. 234–252.

Spalart, P. R., Moser, R. D. & Rogers, M. M. 1991 Spectral methods for the Navier–Stokes equations with one infinite and two periodic directions. *J. Comput. Phys.* **96**, 297–324.

Spalart, P. R. & Watmuff, J. H. 1993 Experimental and numerical study of a turbulent boundary layer with pressure gradients. *J. Fluid Mech.* **249**, 337–371.

Spina, E. F., Donovan, J. F. & Smits, A. J. 1991 Convection velocity in supersonic turbulent boundary layers. *Phys. Fluids* A **3**, 3124–3126.

Spina, E. F., Smits, A. J. & Robinson, S. K. 1994 The physics of supersonic turbulent boundary layers. *Ann. Rev. Fluid Mech.* **26**, 287–319.

Subramanian, C. S. & Antonia, R. A. 1981 Effect of Reynolds number on a slightly heated turbulent boundary layer. *Intl J. Heat Mass Transfer.* **24**, 1833–1846.

Van Driest, E. R. 1951 Turbulent boundary layer in compressible fluids. *J. Aero. Sci.* **18**, 145–160.

Van Driest, E. R. 1955 The turbulent boundary layer with variable prandtl number. In *50 Jahre Grenzshichtforschung* (ed. H. Gortler) Vieweg.

Van Driest, E. R. 1956 On turbulent flow near a wall. *J. Aero. Sci.* **23**, 1007–1011, 1036.

Young, A. D. 1953 Boundary layers. In *Modern Developments in Fluid Dynamics High Speed Flow, Vol. 1* (ed. L. Howarth *et al.*), pp. 375–475. Oxford University Press.

Zeman, O. 1990 Dilatation dissipation: The concept and application in modeling compressible mixing layers. *Phys. Fluids* A **2**, 178–188.